Geophys. J. Int. (1993) **115,** 264–302

Tomographic inversion of *P* and *pP* data for aspherical mantle structure below the northwest Pacific region

R. D. van der Hilst,[1,*] E. R. Engdahl,[2] and W. Spakman[3]

[1]*Department of Earth Sciences, University of Leeds, Leeds LS2 9JT.*
[2]*National Earthquake Information Center, US Geological Survey, DFC, Box 25046, Stop 967, Denver, CO 80225, USA*
[3] *Department of Theoretical Geophysics, University of Utrecht, Budapestlaan 4, 3508 TA Utrecht, The Netherlands*

Accepted 1993 March 15. Received 1993 March 15, in original form 1992 March 6

SUMMARY

To investigate the morphology of subducted slab in the mantle below northwest Pacific island arcs we inverted traveltime residuals for aspherical variations in *P*-wave propagation velocity relative to the radially symmetric iasp91 reference model. The tomographic method used is based on a step-wise linearization of the inversion problem. First, we relocated ISC (International Seismological Centre) hypocentres with re-identified *P* and *pP* phase data using the iasp91 traveltime tables. The variance of *P* residuals relative to iasp91 traveltimes was 17 per cent less than the variance of *P* data reported by the ISC relative to the Jeffreys–Bullen (J–B) traveltime tables. Second, we performed a linearized (LSQR) inversion for Earth structure and source relocation with the *P* and *pP* residuals obtained from the first step, using iasp91 as the reference model for seismic velocities. The incorporation of the depth phase *pP* in the tomographic inversions has two major advantages: (1) the *pP* data provide constraints on focal depth and thus reduce the trade-off between source relocation and structure; and (2) the *pP* ray paths improve the sampling of Earth structure in the shallow mantle and transition zone. We used more than 2×10^6 and about 1×10^5 *P*- and *pP*-wave traveltime residuals, respectively, from about 40 000 earthquakes with epicentres in the study region that were recorded at one or more of the 2300 globally distributed seismological stations considered in this study.

We assessed the spatial resolution in the tomographic images with checker board-type sensitivity tests. These tests reveal high resolution of upper mantle and transition-zone structure, particularly below the central part of our study region. Structure with wavelengths of the order of 100 km is resolved below Japan, whereas structure with wavelengths of the order of 300 km is well resolved below the Kuril, Izu Bonin and Ryukyu arcs. Small-scale structure is poorly resolved in depth below the northern part of the Kuril–Kamchatka arc and below the Izu Bonin and Mariana arcs. This limits the interpretation of slab structure and mantle flow from tomographic images alone.

With this limitation in mind, we conclude from the tomographic images that subducted slab deflects in the mantle transition zone below the geographical area encompassed by the Kuril basin, the Japan Sea, and the northern part of the Philippine Sea. This is in good agreement with the results of other recently published tomographic studies, the occurrence of earthquakes several hundred kilometres off the inclined Wadati–Benioff seismic zones, and inferences about '660 km' discontinuity topography. In contrast, slab-like structures of high *P*-wave velocity are imaged in the lower mantle below the deepest earthquakes of the

* Now at: Australian National University, Institute of Advanced Studies, Research School of Earth Sciences, Canberra ACT 0200. Australia.

northern Kuril–Kamchatka and Mariana seismic zones. This is indicative of local slab penetration of the lower mantle. From tomographic images we cannot discern between compositionally or thermally induced variations in seismic velocity. However, with regard to the nature of the boundary between upper and lower mantle, our observations argue against either compositional mantle layering with large contrasts in intrinsic density or phase changes with steep Clapeyron slopes.

Key words: linearized tomographic inversion, mantle dynamics, Northwest Pacific region, *P* and *pP* phase data, seismic mantle structure, slab deflection and penetration.

1 INTRODUCTION

The subduction of oceanic lithosphere in the Earth's mantle is an important driving mechanism of plate tectonics. Detailed knowledge of the morphology of subduction zones is important to understand better the process of subduction, the relationship between subducted lithosphere and subduction-zone seismicity, and the relation between plate tectonics and mantle convection. Of particular interest is the depth to which subducted lithosphere penetrates into the Earth's mantle. The controversial issues concerning the amount of mass transport between the upper and lower mantle are reviewed by Silver, Carlson & Olson (1988), Olson, Silver & Carlson (1990), and Davies & Richards (1992). With regard to the seismological evidence for (or against) slab penetration into the lower mantle the discussion has been focused on northwest Pacific island arcs, below which fast subduction of old oceanic lithosphere of the Pacific Plate has occurred since the Eocene (Seno & Maruyama 1984) (Fig. 1).

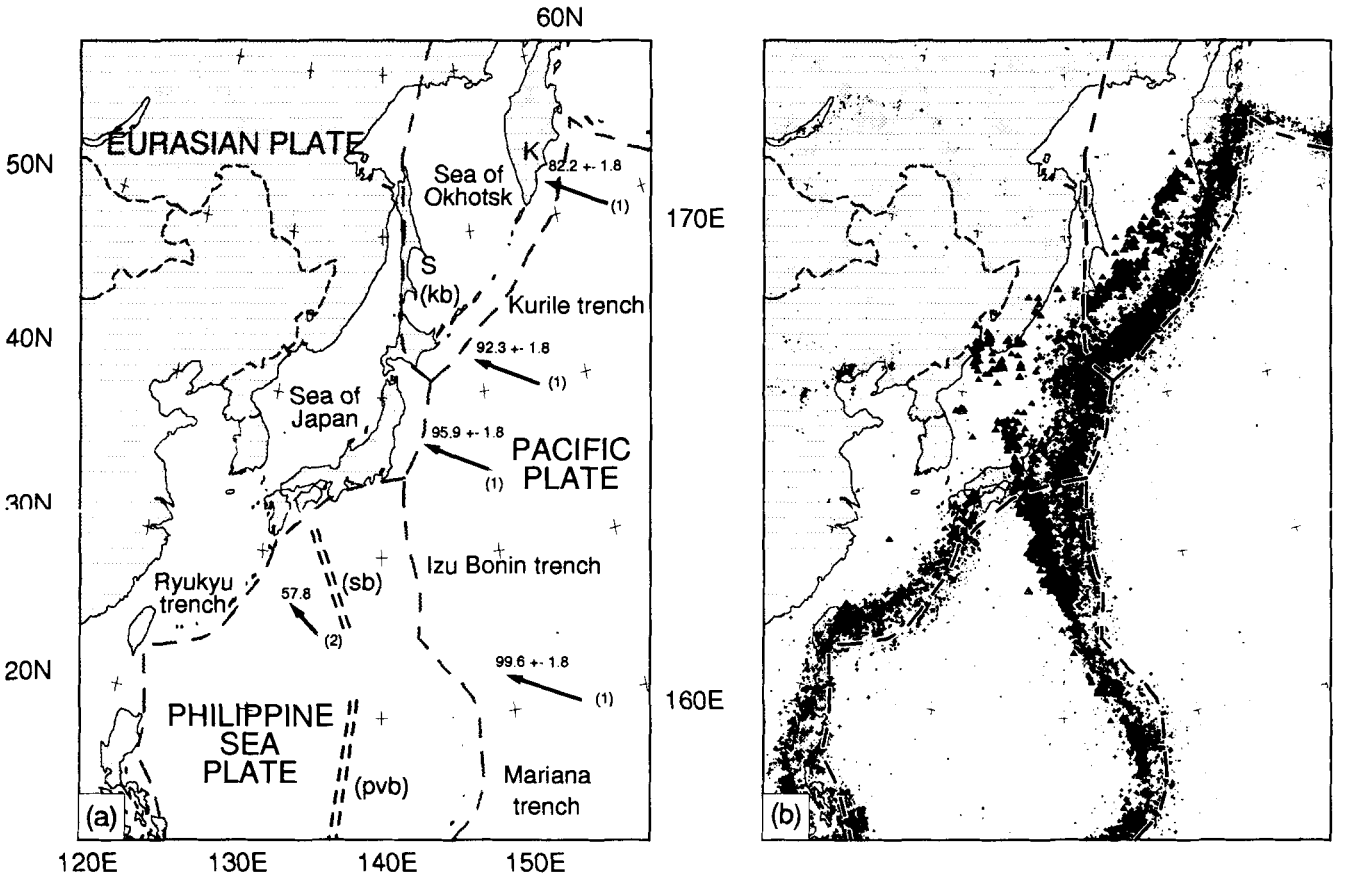

Figure 1. (a) Tectonic map of the northwest Pacific region. Single dashed lines depict plate boundaries after NUVEL-1 (DeMets *et al.* 1990); double dashed lines depict extinct spreading ridges of Shikoku and Parece Vela basins. Explanations of abbreviations used: K = Kamchatka, kb = Kuril basin, pvb = Parece Vela basin, RA = Ryukyu arc, S = Sakhalin island, sb = Shikoku basin. The arrows show direction and rate of relative plate motion. The number at the head of each arrow gives the rate in mm yr^{-1}; the number at the tail corresponds to the type of information used to calculate rate and direction of relative motion. (1) Pole of rotation between the Pacific and Eurasian (fixed) plates after DeMets *et al.* (1990); and (2) the pole of rotation between the Philippine and Eurasian plates after Seno *et al.* (1987). (b) Epicentres of earthquakes with $m_b > 4.0$ that occurred between 1964 and 1989. Locations after ISC. Small dots, crosses, and solid triangles depict epicentres of shallow- ($0 < z < 70$ km), intermediate- ($70 < z < 300$ km), and deep-focus earthquakes, respectively, where z is the focal depth.

Subduction-zone seismicity can be used to delineate subducted lithosphere (e.g. Chiu, Isacks & Cardwell 1991), but possible lower mantle continuations of slabs are aseismic. Lithospheric slab in the lower mantle can produce thermal perturbations and a variation in seismic velocity that can potentially be detected from the traveltimes of transmitted seismic waves. Several investigators have used tomographic methods to resolve northwest Pacific mantle structure with wavelengths of the order of 100 km (Hirahara 1977; Hirahara & Mikumo 1980; Nakanishi 1985; Zhou 1988; Kamiya, Miyatake & Hirahara 1988; Takei & Suetsugu 1989; Suetsugu 1989; Spakman *et al.* 1989; Zhou & Clayton 1990; Zhou, Anderson & Clayton 1990). In spite of these efforts, the tomographic images have not led to unequivocal models of deep slab structure below northwest Pacific island arcs. The published results are irreconcilable, in particular, with regard to slab morphology across the mantle transition zone (410–660 km). Moreover, Spakman *et al.* (1989) have demonstrated that deep slab structure below northwest Pacific island arcs is poorly resolved by the tomographic inversion of *P*-wave traveltime residuals alone.

A trivial source of ambiguity in the results is the use of different subsets of the available seismic data. Kamiya *et al.* (1988) used only teleseismic *P*-wave data to circumvent the complications of computing ray paths bottoming near seismic discontinuities, and the higher noise level of *P*-wave arrival times reported from stations in the triplication range. By restricting the data set to *P*-wave ray paths with small ray parameters, they emphasized deep, steeply dipping structures and may have overlooked possible aseismic, subhorizontal continuations of subduction zones. In contrast, in their northwest Pacific study Zhou and co-workers preferred to avoid the problems of *P* waves travelling outside the parameterized mantle volume. They used mainly data from *P* waves that bottom in the upper mantle and only a few teleseismic rays (Zhou 1988; Zhou & Clayton 1990). As a consequence, their results emphasized upper mantle structure and, particularly in the transition zone, subhorizontal structures. In this study, we inverted traveltime residuals from stations at both regional and teleseismic distances.

More fundamental ambiguities result from differences in the way seismologists handle the non-linearity of the tomographic inversion problem. In tomographic studies, the traveltime inversion is usually linearized, applying Fermat's Principle, about reported trial solutions for source locations and a reference model for seismic velocity (Aki, Christoffersson & Husebye 1977; Aki & Richards 1980; Nolet 1985). This linearization is not trivial. Furthermore, the system of linear equations describing the tomographic problem is inconsistent due to errors in the data, and is usually ill conditioned because of the uneven sampling of Earth structure by seismic wave ray paths. As a consequence, the way in which the traveltime residuals can be explained in terms of hypocentre mislocation and aspherical variation in seismic structure along the ray paths is not unique (Nolet 1985, 1987; Van der Sluis & Van der Vorst 1987).

Van der Hilst & Spakman (1989), Zielhuis, Spakman & Nolet (1989), and Van der Hilst *et al.* (1991) have discussed the importance of the reference model, in particular, when Earth structure in the transition zone is studied. If the effects on the tomographic images of the use of an inadequate reference model are not reduced, or at least recognized, one can easily misinterpret subhorizontal structures in the vicinity of steeply dipping features as 'slab fingering'. We reduced non-linear effects by using a radially stratified reference model that appropriately describes the variation of seismic velocity with depth below the northwest Pacific region: the iasp91 model for *P*- and *S*-wave velocities (Kennett & Engdahl 1991; Kennett 1991).

Another problem in the linearization of the traveltime problem is the quality of the reported reference hypocentre locations. In its earthquake location procedure the International Seismological Centre (ISC) uses *P*-wave arrival times and the Jeffreys–Bullen (J–B) traveltime tables (Jeffreys & Bullen 1967; Adams, Hughes & McGregor 1982). Lateral variation in seismic structure and the uneven spatial distribution of seismological stations can easily combine to produce earthquake mislocations of several tens of kilometres (Engdahl, Sleep & Lin, 1977; Engdahl, Dewey & Fujita, 1982; Dziewonski & Anderson 1983; Nieman, Fujita & Rogers 1986). Such mislocations can result in non-linear effects, such as the misidentification of seismic phases and the loss of structural signal in the data (Van der Hilst & Engdahl 1992; Engdahl, Buland & Van der Hilst 1993), and there is a danger of mapping biases in hypocentre location into the solution of seismic inversion. These problems in the routinely reported data motivated us to relocate ISC earthquake hypocentres prior to tomographic inversion. In the subsequent linearized inversion we used the new trial locations and inverted simultaneously for Earth structure and small mislocations due to lateral heterogeneity. To reprocess arrival-time data for northwest Pacific hypocentres with the iasp91 reference model we used software developed by Buland & Chapman (1983) for the rapid computation of traveltimes and derivatives. The reprocessing is discussed by Van der Hilst & Engdahl (1992) and, in more detail, by Engdahl *et al.* (1993).

We showed elsewhere that the variance of the *P*-wave traveltime residuals for earthquakes relocated with iasp91 is about 17 per cent less than the scatter of ISC *P*-wave data (Van der Hilst *et al.* 1991; Engdahl *et al.* 1993). This difference in data variance is of the same order as the variance reduction that is typically obtained upon tomographic inversion of ISC *P* data. This demonstrates the danger that the part of the signal in ISC *P* data that is actually due to event mislocation or errors in the J–B traveltime tables can be mapped incorrectly into Earth structure (Van der Hilst *et al.* 1991). Hereafter, Van der Hilst *et al.* (1991) and Engdahl *et al.* (1993) are referred to as 'NWP1' and 'NWP2', respectively.

In NWP1 we discussed important implications of the incorporation of data of the surface-reflected *pP* phase in both the relocation procedure prior to inversion and in the subsequent simultaneous inversion for source location and Earth structure. The incorporation of *pP* data in the tomographic inversion gives better constraints on focal depth (Van der Hilst & Engdahl 1992; NWP2), which significantly reduces the trade-off between source relocation and amplitudes of imaged variation in seismic velocity. The inversion of our new data set resulted in images with contrasts in seismic velocity between slab structure and the surrounding mantle larger than previously reported. The

new images are indicative of slab penetration below some island arcs and upper mantle slab deflection below others. The inversion of uncorrected ISC *P* data results in long slabs, the depth extent of which is not well resolved (Spakman *et al.* 1989), and low contrast between seismic velocity in the slab and the surrounding mangle (NWP1).

Here, we present the complete solution of the inversion of our northwest Pacific *P* and *pP* data set, and the results of resolution tests, and discuss implications for our perception of mantle dynamics. Detailed interpretations of the inversion results in the context of regional tectonics will be published elsewhere (Van der Hilst & Seno 1993).

2 METHOD

The tomographic method used in this study is based on the LSQR inversion algorithm of Paige & Saunders (1982) which is described in detail by Nolet (1985), Van der Sluis & Van der Vorst (1987), Spakman (1988), and Spakman & Nolet (1988). In our application, we used explicit regularization (damping) to stabilize the solution in poorly sampled mantle regions (Van der Sluis & Van der Vorst 1987; Spakman & Nolet 1988). The traveltime residuals are inverted for the variation in *P*-wave propagation velocity in the mantle volume under study, for effects on traveltime of source mislocation due to the presence of lateral heterogeneity, and for delays acquired along ray path segments outside the parameterized mantle volume (Spakman & Nolet 1988).

The incorporation of data from later-arriving seismic phases, like *PP* and *pP*, in delay-time tomography was discussed by Van der Hilst & Engdahl (1991); the data processing and earthquake relocation procedure is discussed in NWP2 and by Van der Hilst & Engdahl (1992). In the present paper, we address only those aspects of the method that are specifically applied to the northwest Pacific region—notably the parameterization—and the most important differences with respect to other tomographic studies of northwest Pacific mantle structure. The following aspects of our method are discussed in this paper:

(1) the parameterization of the aspherical Earth structure in the mantle volume under study with non-overlapping cell slowness functions (Nolet 1985; Spakman & Nolet 1988).

(2) The use of the iasp91 model for *P*- and *S*-wave velocities (Kennett & Engdahl 1991; Kennett 1991) as the reference model (instead of the commonly used J–B model).

(2) The use of earthquake hypocentres which are initially located in the iasp91 model (instead of the hypocentral parameters published by the ISC).

(4) The assessment of the reliability of the tomographic images with resolution tests as described by Spakman & Nolet (1988).

2.1 Parameterization with non-overlapping cells

In our study of the aspherical variation of *P*-wave velocity in the mantle below the northwest Pacific region we used a parameterization with slowness block functions (*cf.* Nolet 1985). Inside each block the slowness is assumed to be constant. Outside of the parameterized mantle volume we assumed the reference earth model.

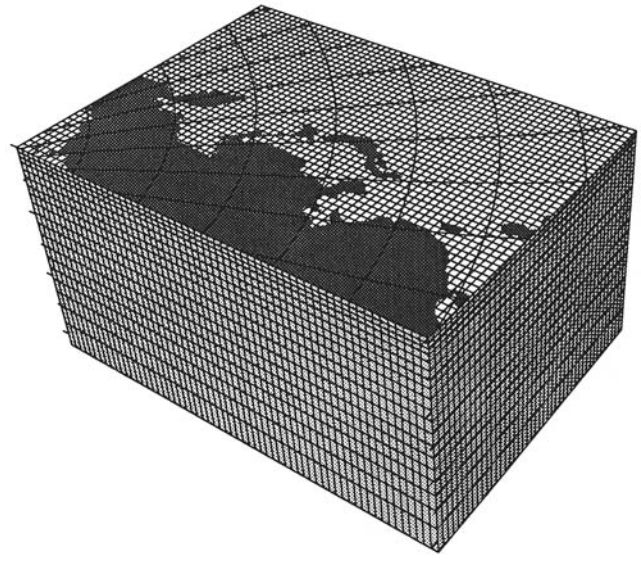

Figure 2. Model of non-overlapping blocks used for the parametrization of the mantle volume under study.

The parameters describing the cell model (shown in Fig. 2) are the same as used in an earlier study (Spakman *et al.* 1989). The horizontal dimensions of the blocks are $1° \times 1°$, and the thickness of the layers varies from 33 km for the uppermost layer to 200 km for the deepest layer centred at 1500 km depth (Table 1). The block model is rotated clockwise over 35° relative to geographical north in order to encompass the largest possible seismic region with a certain number of blocks (*cf.* Spakman 1988, 1991). The parameterization involves 48 750 blocks. In Section 4 of this paper the variation in seismic velocity is presented for each of the 19 layers of the model shown in Fig. 2.

Table 1. Information about the cell model.

layer	depth range (km)	P-wave velocity (km/sec) (layer average - iasp91)	Average anomaly (%) (relative to iasp91)
1	0- 35	6.102	+0.06
2	35- 70	8.042	-0.11
3	70- 110	8.047	-0.09
4	110- 160	8.095	-0.06
5	160- 220	8.245	-0.14
6	220- 280	8.445	-0.23
7	280- 340	8.664	-0.17
8	340- 410	8.902	-0.18
9	410- 490	9.494	+0.11
10	490- 570	9.763	+0.26
11	570- 660	10.049	-0.04
12	660- 750	10.909	-0.16
13	750- 840	11.116	-0.16
14	840- 930	11.274	-0.17
15	930-1020	11.423	-0.20
16	1020-1130	11.582	-0.23
17	1130-1250	11.756	-0.20
18	1250-1400	11.948	-0.18
19	1400-1600	12.184	-0.11

2.2 Linearization of the inversion

The non-linear problem of determining Earth structure by traveltime inversion is usually linearized about a reference velocity model and source locations with the following assumptions (e.g. Bolt 1960; Buland 1976; Aki & Richards 1980; Spakman 1988, 1991). First, the reference earth model must be sufficiently close to the true Earth so that we can apply Fermat's Principle. Secondly, (*cf.* Aki & Richards 1980) for each earthquake the trial solution for hypocentre location $\hat{\mathbf{x}}_0$ must be sufficiently close to the true location $\mathbf{x}_0$ so that the change in traveltime of a seismic wave from source to station due to small perturbations in the hypocentral parameters is virtually unchanged between $\hat{\mathbf{x}}_0$ and $\mathbf{x}_0$. In this section we show that neither assumption is trivial.

2.2.1 *The reference model of seismic velocities*

The choice of a reference model is important. Van der Hilst & Spakman (1989) and Zielhuis *et al.* (1989) showed by comparison of ray paths computed by ray tracing in candidate 1-D reference models—for instance J–B and PEM (Dziewonski, Hales & Lapwood 1975)—that the uncertainty in ray paths for seismic waves bottoming in the upper mantle can be as large as 200 km. The use of a model that does not adequately describe the average seismic properties in the Earth's interior would result in the violation of one of the assumptions underlying the linearization.

Most reference models used in large-scale tomographic studies are spherically symmetric with the propagation velocity of seismic waves varying only with depth. Ideally a laterally heterogeneous earth model should be used as the initial model, with the reference ray paths computed by 3-D ray tracing. In recent papers, Zhao, Horiuchi & Hasegawa (1990) and Hasegawa *et al.* (1991) demonstrated what can be achieved by non-linear inversion of high quality data. However, 3-D ray tracing is very time consuming—although fast ray tracers are being developed (Moser 1991)—and still prohibitive when dealing with millions of data and model spaces that are one or two orders of magnitude larger than in Hasegawa *et al.* (1991). The use of fixed reference ray paths, determined by shooting in an adequate 1-D reference model, would be justified if the contribution of unknown deviations from 1-D structure to the uncertainty in ray path is large as compared to the effect of lateral heterogeneity. We assume that with the parameterization described above—the coarseness of which is dictated by the quality of the seismic data—this is indeed the case.

Van der Hilst & Spakman (1989) and Zielhuis *et al.* (1989) determined reference models from the traveltime residuals subsequently used in the tomographic inversions. In contrast, we decided to use an existing global velocity model, the iasp91 model for *P*- and *S*-wave velocities (Kennett & Engdahl 1991; Kennett 1991) (Fig. 3). This has the advantages that it is developed independently of our study, that software, e.g. for the rapid computation of traveltimes is readily available, and that such a model could easily be used by other investigators, which would facilitate the comparison of tomographic images. Moreover, although a regional model could represent the average *P*-wave velocity better than iasp91, the effect of small changes in the starting model on the reference ray paths would probably be of the same order of magnitude as that of unknown lateral heterogeneity. This makes efforts to use a slightly different radially stratified model than iasp91 futile.

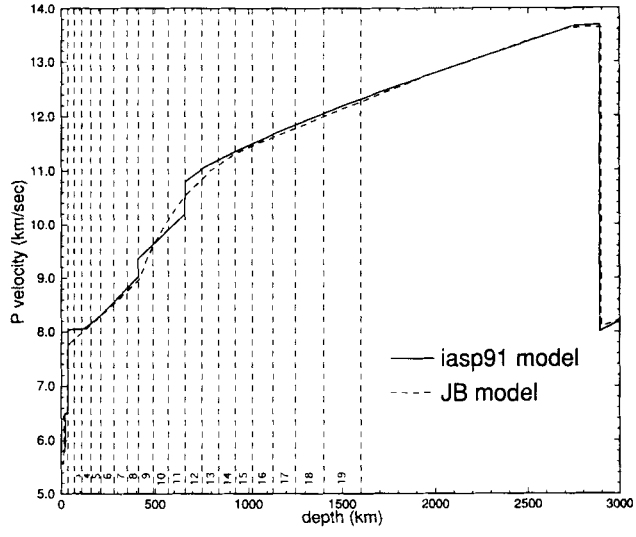

Figure 3. The J–B and iasp91 models for *P*-wave velocity. Dashed lines are drawn at the depths of layer boundaries in the block model.

For each layer of the block model (Fig. 2) the average iasp91 *P*-wave velocity is given in Table 1. We showed elsewhere (NWP1 and NWP2) that the variance of the *P*-wave data computed with iasp91, and earthquake hypocentres located therein, is about 17 per cent less than the variance of ISC *P* residuals computed from the J–B traveltime tables (Jeffreys & Bullen 1967). There are at least two good reasons to believe that the difference in variance is mainly due to differences in the iasp91 and J–B traveltime tables. First, the reduction is comparable in magnitude to the reduction obtained by Van der Hilst & Spakman (1989), who corrected for a reference model other than J–B without the relocation of earthquake hypocentres in the new model. Second, hypocentre relocation alone would not result in a significant reduction of variance of ISC *P*-wave data. The ISC *P*-wave data are optimal with respect to the ISC reported hypocentre parameters—indeed, they are the residuals of the ISC least-squares earthquake location (Adams *et al.* 1982)—and changes in hypocentre location would result in an increase of data variance rather than a reduction.

The presence (or absence) of seismic discontinuities in the reference model has a large effect on the reference ray paths (Grand 1987; Zielhuis *et al.* 1989; Van der Hilst & Spakman 1989) and, hence, on the effective sampling of structure in the transition zone. Ray theory predicts no first-arriving *P* waves with ray paths that bottom just above the seismic discontinuities. Indeed, Van der Hilst (1990) showed from mapping the number of ray paths that sample a particular block (the hit count) that mantle regions just above the '410' and '660' km discontinuities are less often sampled by ray paths of first-arriving *P* waves than Earth structure elsewhere (Fig. 4). The use of models like PREM (Dziewonski & Anderson 1981) and iasp91 (Kennett & Engdahl 1991) would thus result in an uneven sampling of

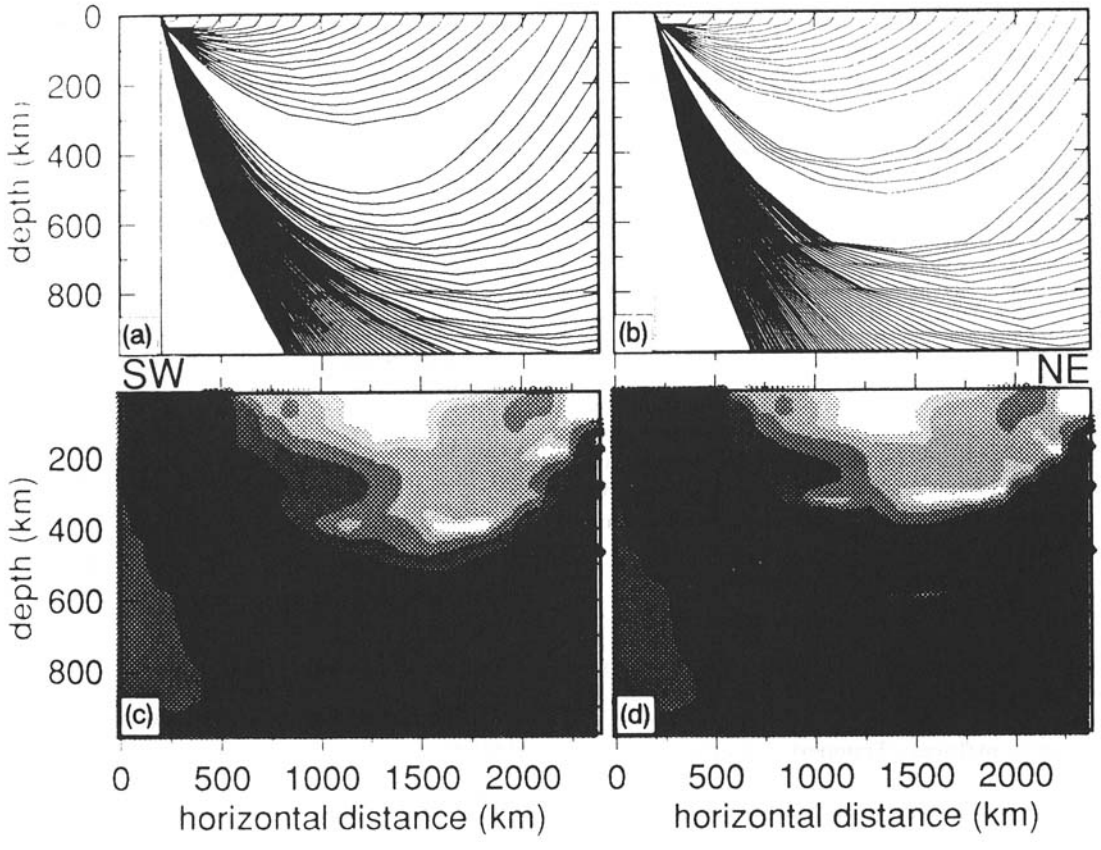

Figure 4. Inhomogeneous distribution of reference ray paths due to the first-order seismic discontinuities or strong velocity gradients in the reference model. We computed ray paths in the J–B (a) and VCAR (b) reference models by 1-D ray tracing. The *P*-wave velocity model VCAR, which was derived by Van der Hilst & Spakman (1989) for a tomographic study of mantle structure below the Caribbean, has seismic discontinuities at 390 and 660 km. We illustrate the sampling of mantle structure by ray paths used in the Van der Hilst & Spakman study by means of a cross-section through a 3-D model of hit count (*cf.* Section 4.1.2. of the text). (c) Sampling by reference ray paths determined with the J–B model. (d) Ibid. for reference ray paths computed in VCAR. The presence of mantle discontinuities in the model VCAR results in the inhomogeneous sampling of transition zone structure.

structure in the upper mantle and transition zone (Fig. 4). In contrast, the use of J–B—without a '660' km discontinuity—would result in a more homogeneous spatial distribution of reference ray paths and an apparently better sampling of structure, particularly in the transition zone. (This topic is also discussed in Section 2.3.1). The sampling of structure in the transition zone can potentially be improved by using later-arriving *P* waves associated with triplication branches (Remkes & Spakman 1992) or phases such as *pP* (this study) and *PP* (Van der Hilst & Engdahl 1991).

2.2.2 Step-wise hypocentre relocation

Lateral variation in seismic structure, the uneven spatial distribution of seismological stations, and the specific choice of seismic data used to determine the earthquake hypocentres can combine to produce earthquake mislocations of several tens of kilometres (Engdahl *et al.* 1977, 1982; Dziewonski & Anderson 1983; Nieman *et al.* 1986; NWP2). The condition for linearization given above can be satisfied even for substantial mislocations, because the hypocentre partial derivatives could be approximately the same for the true and the mislocated source, but such large mislocations give rise to various non-linear effects on the reported phase data. There is a real danger that seismic phases are misidentified, and that structural signal is lost in the phase data. For seismic velocities typical for the upper mantle a mislocation in focal depth of 10 km is equivalent to a teleseismic traveltime residual of 0.5 to 1.0 s, or a near-source velocity anomaly of several per cent. The value of phase data from biased hypocentres in constraining seismic images is thus significantly reduced.

An important novel aspect of our method is the attempt to obtain reference hypocentres adequate for linearized inversion, and to recover lost structural signal, by the relocation of ISC earthquake hypocentres prior to tomographic inversion using ISC *P*- and *pP*-wave arrival times and the iasp91 traveltime tables. The step-wise relocation procedure that underlies our linearized tomographic inversion is described in detail in NWP2 and is summarized by Van der Hilst & Engdahl (1992).

2.3 Assessment of reliability of the images: resolution tests

The interpretation of tomographic images is complicated by the presence of artefacts owing to inadequate sampling of structure by ray paths, incorrect *a priori* assumptions, i.e.

the reference model and source locations, and undesirable properties of the numerical algorithms used to solve the inversion problem (Spakman & Nolet 1988; Van der Hilst & Spakman 1989; Spakman *et al.* 1989). Here we follow Spakman & Nolet (1988) and Humphreys & Clayton (1988) and assess the resolution with sensitivity tests, which serve the same purpose as the 'checker board tests' used by Inoue *et al.* (1990) and Fukao *et al.* (1992).

In sensitivity tests, synthetic traveltime residuals are computed for an input model with known variations in seismic velocities (*cf.* Sections 4.1.3 and 4.1.4 of this paper, Spakman & Nolet 1988) using the same ray paths as in the inversion of reported traveltime residuals. Gaussian noise is added to the synthetic data. The fit between the input model and the inversion response to this model is used to assess how well the combination of the particular numerical code and the suite of ray paths used in the inversion retrieves information about Earth structure from noisy seismic data (Spakman & Nolet 1988).

2.3.1 Limitations of 'checker board' resolution tests

It is important to realize that the diagnostic value of 'checker board' resolution tests is limited. The resolution as assessed from 'checker board' tests or from formally computed resolution matrices (Trampert & Leveque 1990) only reveals how well the tomographic system of linear equations is solved. It does not test the degree of non-linearity or the accuracy of the linearization approximations. Also, these tests do not account for parameterization effects, such as spatial aliasing, because the input models are usually expanded in terms of the same basis vectors as in the inversion of reported data.

There are essential differences between the linearized inversion of reported phase data for unknown structure and the inversion of data computed from a known model of seismic velocities. First, in synthetic data there is no problem with phase misidentification, or biases due to mislocation of earthquake hypocentres (*cf.* Section 2.2.2). Second, possible systematic errors in reported data (e.g. misidentified late arrivals in the triplication range, and effects of station characteristics (Grand 1990)) are not modelled by sensitivity tests. Third, 'checker board' tests do not reveal inadequacies of the linearization about the reference velocity model used, because the synthetic data are always consistent with the reference ray paths. With regard to the quality of the reference model there can be a paradoxal relationship between the apparent resolution determined from sensitivity tests and the reliability of the solution. For instance, the use of a relatively simple reference model can produce an even distribution of reference ray paths which facilitates seismic imaging. In contrast, in a reference model that more adequately represents the average seismic velocity in the Earth's interior (like iasp91) the spatial distribution of reference ray paths can be complex, and the sampling of structure in the upper mantle and transition zone uneven (Fig. 4), which severely degrades the tomographic imaging. Hence, in a linearized inversion the use of the most appropriate reference model does not necessarily give the best resolution in terms of the results of 'checker board tests', but it would produce a more reliable solution.

3 THE SEISMIC DATA

3.1 The choice of seismic data

To ensure the adequate sampling of both upper and lower mantle structure, we used *P*-wave traveltime residuals from stations at epicentral distances from 0° to 95°. In addition, we used *pP*-wave traveltime residuals from stations between 25° and 90° epicentral distance. The advantages (and disadvantages) of the incorporation of *pP* data in the inversion are reviewed by Van der Hilst & Engdahl (1991, 1992) and in NWP2. The higher noise level of *P* data at regional distances and *pP* data is accounted for by weighing the phase data (*cf.* Section 3.6).

In contrast to our study of Caribbean mantle structure (Van der Hilst 1990; Van der Hilst & Engdahl 1991) we did not incorporate data of the surface reflected *PP* phase. Routinely reported *PP*-phase onsets are not corrected for effects of waveform distortions and are much noisier than *pP* data (Van der Hilst & Engdahl 1991). For our study region, mantle regions that would be sampled by *PP*-wave ray paths are sampled effectively by *pP*-wave ray paths.

3.2 The distribution of earthquakes and seismological stations

In this study we used *P*- and *pP*-wave traveltime residuals from earthquakes located in the geographical area bounded by 110 °E and 180° in longitude, and 5 °N and 75 °N in latitude. The epicentres are shown in Fig. 1(b). The arrivals of the *P* and *pP* phases are recorded at one of the nearly 2300 (globally distributed) seismological stations that reported to the ISC between 1964 and 1987 and the National Earthquake Information Center (NEIC) from 1987 to 1989.

For the selection of earthquakes we did not impose limits on the magnitude, focal depth, or the number of recording stations. Instead, we only considered data from earthquakes with epicentres within the region under study and with a calculated location error less than 25 km (NWP2). The reported magnitudes of the earthquakes that passed the selection procedure range between 3.0 and 7.0, but we also included data from earthquakes for which no magnitude was reported by the ISC and NEIC (Fig. 5).

From outside the study region, 1961 stations contributed over 70 per cent of the data used in our study. Most of these stations are located in Europe or in North America (Fig. 6a). Fig. 6(b) shows the distribution of the 323 contributing stations located in the study region.

3.3 The NWP *P* data

We only address the *P* and *pP* data computed with the relocated hypocentres and the iasp91 model of seismic velocities: this data set will hereafter be referred to as NWP *P* and *pP* data. Information about reported ISC/NEIC *P* and *pP* data is given for comparison only.

In Fig. 7(a) reported ISC/NEIC *P*-wave traveltime residuals are plotted versus epicentral distance. This way of displaying the data is instructive, in particular to discuss the reference model (Van der Hilst & Spakman 1989; Zielhuis *et al.* 1989; NWP1). In Fig. 8(a), the frequency distribution

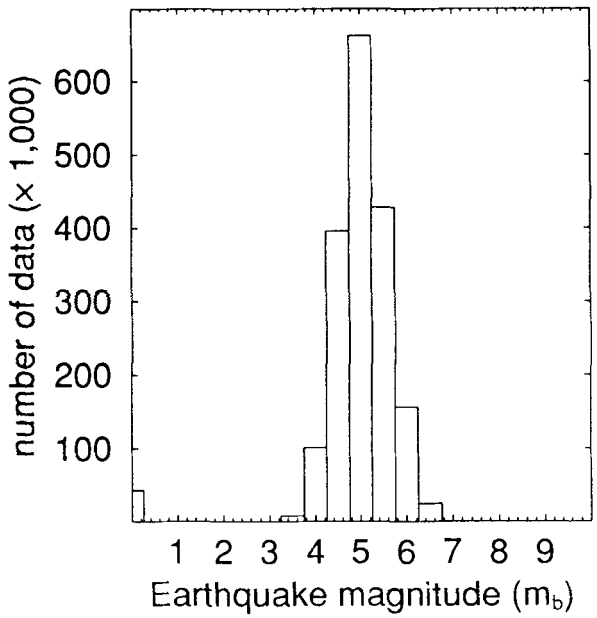

Figure 5. Frequency distribution of the number of *P*-wave data used versus earthquake (body wave) magnitude.

of ISC *P* residuals (with absolute values less than 7.5 s) is given. The distribution of 2 105 399 ISC/NEIC *P* data has a mean of −0.03 s and a standard deviation σ of 1.47 s (variance σ^2 is 2.16 s^2). The application of the selection criteria listed in Table 2 (RUN 1) resulted in a data set of 2 232 430 NWP *P* residuals. For details of the data processing we refer to NWP2. We note that upon processing, arrivals can be associated to the *P* phase although they were not originally identified as *P* by the ISC. The distribution of NWP *P* residuals versus epicentral distance is given in Fig. 7(b) and the frequency distribution in Fig. 8(b). The distribution of NWP *P* data has a mean 0.11 s and a σ of 1.34 s ($\sigma^2 = 1.80$ s^2). These numbers are obtained from NWP *P* data with absolute values less than 7.5 s in order to enable a direct comparison with the statistics of ISC/NEIC data (Fig. 8a).

In the actual inversion we used composite rays (Spakman & Nolet 1988; Spakman 1988, 1991). We allowed a maximum of 10 rays (from a cluster of earthquakes to a cluster of stations) to contribute to a single composite ray. In this second processing step, RUN 2 in Table 2, *P* residuals with absolute values larger than 7.5 s were rejected. We are aware that with this cut-off we may also have discarded very early arrivals of *P* waves travelling through the slab as observed and discussed by Huppert & Frohlich (1981), Ansell & Gubbins (1986), and Gubbins & Snieder (1991). These early arrivals are, however, due to wave propagation through high-velocity layers with thicknesses probably less than 15 km (Gubbins & Snieder 1991); such thin layers cannot be imaged appropriately by the presently applied tomographic technique. From the *P*-wave ray paths we constructed nearly 1.1E + 06 composite rays and associated data. The distribution of the *P* data versus epicentral distance after RUN 2 is given in Fig. 7(c). In the subsequent tomographic inversions we used 1 059 501 *P* data with absolute values of traveltime residuals less than 5 s.

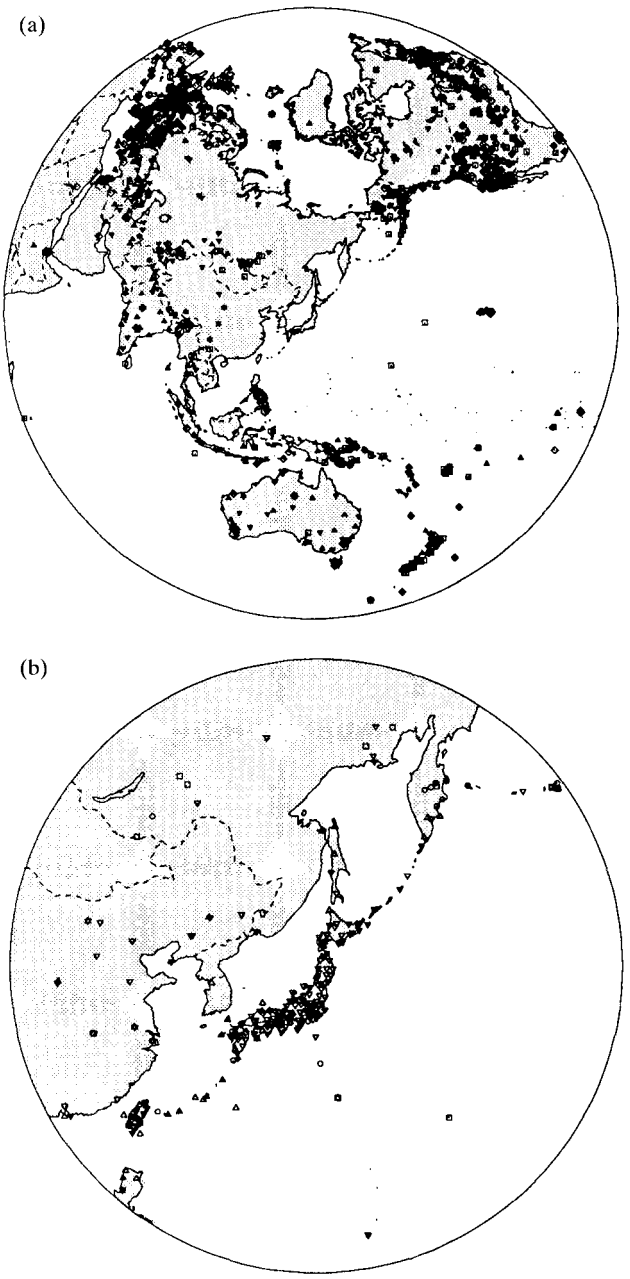

Figure 6. Distribution of the seismological stations that contributed to the data set used in our inversion. (a) Seismological stations located outside the study region. (b) Stations located within the study region.

The frequency distribution of these data (mean = 0.02 s, $\sigma = 1.24$ s, $\sigma^2 = 1.54$ s^2) is shown in Fig. 8(c).

3.4 The NWP *pP* data

The frequency distribution of 78 949 uncorrected ISC *pP* data is given in Fig. 10(a). Fig. 10(a) shows that the distribution of ISC *pP* data is asymmetric and skewed, has a large negative mean value (mean = −0.91 s), and a standard deviation of 2.68 s ($\sigma^2 = 7.18$ s^2).

The criteria used to process *pP* data are given in Table 2, and are discussed in detail in NWP2. We adopted a

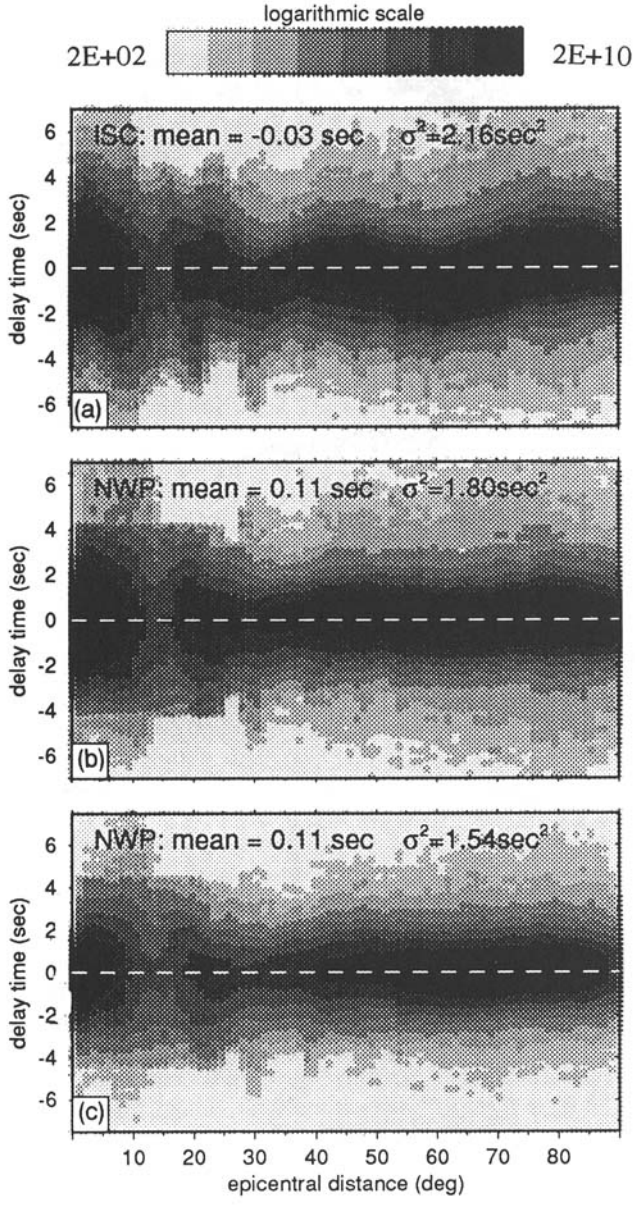

Figure 7. 2-D frequency distributions (logarithmic scale) of *P*-wave traveltime residuals versus distance to epicentres of northwest Pacific earthquakes. (a) *P* residuals relative to J–B traveltimes published by the ISC. (b) NWP *P* residuals relative to iasp91 traveltimes computed from relocated hypocentres (NWP2). (c) NWP *P* residuals after clustering procedure (see text Section 3.3).

minimum focal depth of 35 km for the earthquakes from which we use *pP* data to ensure a large enough separation between *pP*- and *sP*-wave arrival times, and a large enough spacing between *P*- and *pP*-wave ray paths. For focal depths larger than 35 km, we show the distribution of ISC *pP* data versus epicentral distance in Fig. 9(a); the frequency distribution of these *pP* data is given in Fig. 10(b). After the first data processing step (NWP2), the *pP* data are more normally distributed: mean value = 0.07 s, $\sigma = 1.82$ s, $\sigma^2 = 3.31$ s^2. The distribution of the 85 516 NWP *pP* data is given in Figs 9(b) and 10(c). A large number of the NWP *pP* data used in this study were not previously identified as *pP* by the ISC (NWP2).

In the tomographic inversions, we used 66 042 composite *pP* rays with absolute values of the residuals less than 5 s. The statistics of the data used in the inversion are given in Fig. 10(d) (mean = 0.11, $\sigma = 1.81$, $\sigma^2 = 3.28$ s^2).

3.5 The distribution of *pP* reflection points

In Fig. 11 we show the distribution of the reflection points of all *pP*-wave ray paths processed in this study. Compared to the distribution of earthquake epicentres (Fig. 1b) and seismological stations in the region under study (Fig. 6b), the *pP* reflection points are much more evenly distributed, particularly in the northwest Pacific back-arc regions. Most *pP*-wave ray paths used in our study have reflection points in oceanic regions. For high-frequency signals, the air–water interface has a larger impedance contrast than the water–(water saturated) sediment interface and there is a danger that *pP* arrivals read from SPZ records are actually arrivals of the *pwP* phase (see Van der Hilst & Engdahl 1991, for a discussion). Many *pwP* phase arrivals fall outside the adopted time windows (Table 2, and NWP2), but some *pwP* arrivals—misidentified as *pP* arrivals—are still present in our data set (NWP2).

We remark that iasp91 has a distinctly continental character for its uppermost structure (Kennett & Engdahl 1991; Kennett 1992). Because most *pP* reflection points are located in oceanic or marginal sea regions there may be a bias in the imaged seismic structure and the hypocentre locations. This will be discussed in Section 5.2.

3.6 Correction and weighting of the phase data

Ellipticity correction. The NWP *pP*- and *P*-wave traveltime residuals are corrected for Earth ellipticity using the formula given by Dziewonski & Gilbert (1976) (*cf.* Van der Hilst & Engdahl 1991).

Station corrections. To account for structural signal acquired along segments of the reference ray paths outside the parameterized mantle volume (Fig. 2), we computed station corrections (Spakman & Nolet 1988) for all stations located outside the area of interest. If available, we first applied the station corrections published by Toy (1990) to data from stations outside the study region if the epicentral distance is larger than 25°. Toy's corrections result from a study of lower mantle structure and represent delays due to upper mantle structure. The corrections are thus assumed to account for aspherical upper mantle structure outside the model given in Fig. 2. In addition, we inverted for station corrections for all stations outside the study region (Fig. 6a). For stations for which Toy's corrections were available, this additional correction is invoked to correct for aspherical lower mantle structure outside the mantle volume under study, and for effects of sampling near-receiver structure in a limited range of directions and take-off angles.

Topography corrections. The *pP* traveltimes are corrected for water depth above the reflection points (Van der Hilst & Engdahl 1991; Paper 2). We used a topography file

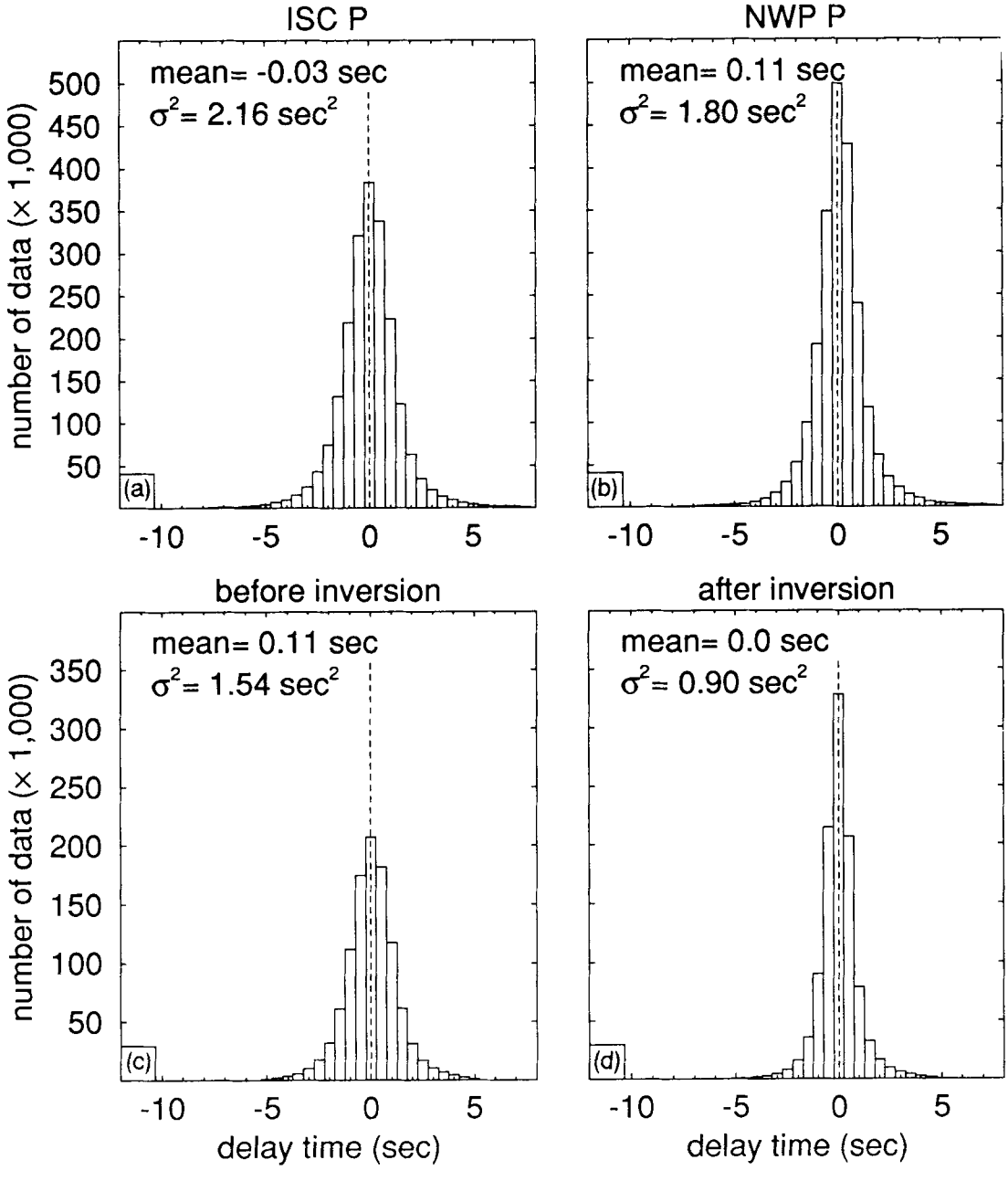

Figure 8. Frequency distributions of *P*-wave traveltime residuals. (a) ISC *P* delay times. (b) *P* delays after reprocessing of ISC hypocentres (NWP2). (c) *P* delay times (composite) after clustering procedure which are used as input to the tomographic inversions. (d) *P*-wave residuals after inversion with the LSQR algorithm (35 iterations).

Table 2. Selection criteria *P* and *pP* data.

	RUN 1 (NWP2)		RUN 2 (composite rays)	
	P data	pP data	P data	pP data
min. and max. latitude	5° N - 75° N	5° N - 75° N	(within block model of Fig. 2)	
min. and max. longitude	110° E - 180° E	110° E - 180° E	(within block model of Fig. 2)	
distance range [deg]	0 - 90	25 - 100	0 - 90	25 - 105
focal depth range [km]	> 0	> 35	> 0	> 35
min. event magnitude	0	0	0	0
min. number obs. per event	1	1	1	1
delay time window [sec]	[-15,+15]	[-15,+15]	[-7.5,+7.5]	[-7.5,+7.5]
number of data	2.2E+06	7.9E+04	1.8E+06	8.6E+04
max # rays in composite ray	(N/A)	(N/A)	10	10
# composite rays	(N/A)	(N/A)	1.1E+06	6.6E+04

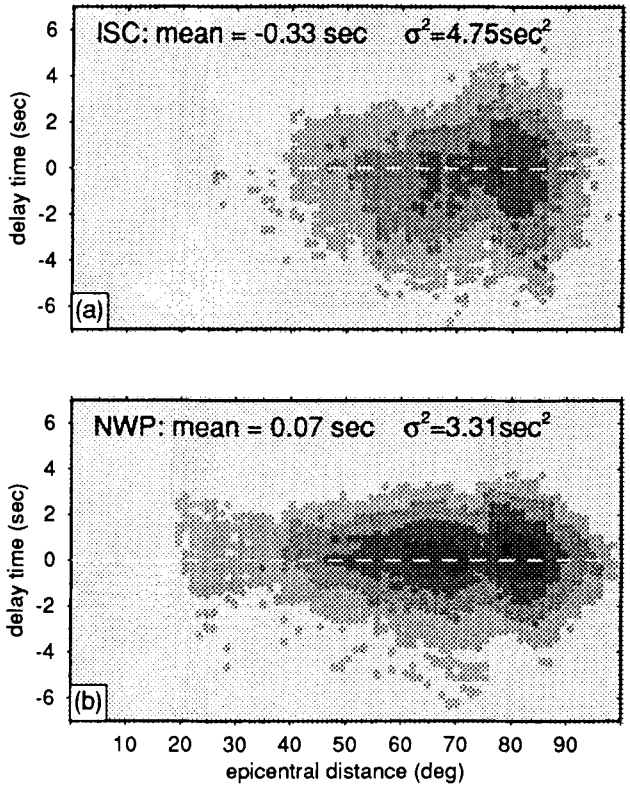

Figure 9. 2-D frequency distributions (logarithmic scale) of *pP*-wave traveltime residuals versus distance to epicentres of northwest Pacific earthquakes with focal depths exceeding 35 km. (a) *pP* residuals relative to J–B traveltimes published by the ISC. (b) NWP *pP* residuals relative to iasp91 traveltimes computed from relocated hypocentres (NWP2).

extracted from the $5' \times 5'$ grid file of the National Oceanic and Atmospheric Administration.

In contrast to the study for mantle structure below Central and South America (Van der Hilst 1990), traveltime residuals used here are not corrected for station elevation. The effect on *P*-wave traveltime of elevation of the stations in the study region (Fig. 6b) would not be significant, and for stations outside the region (Fig. 6a) we assume that the station corrections computed upon inversion account for effects of station altitude.

Weighting. The *P* and *pP* data are weighted by the reciprocal of the estimated noise variance in each of these data (Van der Hilst & Engdahl 1991). For the noise in *P* data we estimated a variance σ^2_{noise} of $1.0\,s^2$ ($1.7\,s^2$ for regional *P* data), and for the noise in the *pP* data σ^2_{noise} is estimated to be $2.25\,s^2$. These estimates of the variance of the noise in the NWP *P* and *pP* data are also used for the addition of normally distributed noise to the synthetic data computed in the resolution tests (*cf.* Sections 4.1.3 and 4.1.4).

4 RESULTS OF THE TOMOGRAPHIC INVERSIONS

The tomographic images presented in this paper are obtained after 30 iterations of the inversion based on the LSQR algorithm (Paige & Saunders 1982; Nolet 1985; Van der Sluis & Van der Vorst 1987; Spakman & Nolet 1988). In the inversions we used 1 059 501 *P* and 66 042 (composite) *pP* ray paths and data (*cf.* Sections 3.3 and 3.4). The traveltime residuals are truncated within the residual interval of $[-5, +5]$ sec. The frequency distributions of the *P* and *pP* residuals after inversion are given in Figs 8(d) and 10(e), respectively. Upon inversion of *P* and *pP* residuals the variance reductions obtained with respect to the input data are 41.6 per cent and 21.0 per cent for *P* and *pP* residuals, respectively. The variance reduction for the combined data set is 37.1 per cent. Upon inversion of *P*-wave data only the variance reduction is 41.9 per cent. Thus, the addition of *pP*-wave ray paths only slightly decreases the ability of the algorithm to fit the *P* data. The reduction of residual variance versus the number of iterations is given in Fig. 12 for the inversion of *P*-wave data alone and for the inversion of the combined data set.

In Section 4.2 we discuss that part of the solution concerned with the aspherical variation in *P*-wave velocity. The relocation parameters and station corrections are briefly discussed in Section 4.3. Van der Hilst & Engdahl (1992) compare in detail the relocation parameters computed before and upon tomographic inversion. Only the solution for the inversion of NWP *P* and *pP* data is given. Important differences between results of the tomographic method discussed in this paper and the results of the straightforward inversion of ISC *P* data, with J–B as the reference model, are discussed in NWP1.

4.1 Presentation of the tomographic images

For the layers of the block model shown in Fig. 2 we display in Figs 14 and 15 the images of aspherical variation in seismic velocity, the sampling of mantle structure by *P*- and *pP*-wave ray paths, and the results of resolution tests. In Fig. 13 we present the distribution of earthquake hypocentres in the lithosphere, upper mantle and transition-zone depth intervals encompassed by layers of the block model (Table 1, Fig. 2). Figs 1 and 13(a) provide us with a geographical reference for the description of the tomographic images. In Figs 14 and 15 we display the results for the depth intervals 0–660 km and 660–1600 km, respectively.

4.1.1 Aspherical variation in P-*wave velocity*

Figures 14[1–11](a) and 15[12–19](a) depict lateral variations in the propagation velocity of longitudinal (*P*) waves relative to the layer averages of the iasp91 *P*-wave velocity model (Table 1). The dark (light) colours depict mantle regions with *P*-wave propagation faster (slower) than iasp91 model. Velocity variations up to 3.5 per cent (in Fig. 14; 2.1 per cent in Fig. 15) relative to iasp91 are given, although higher values do exist in some regions (as will be pointed out in the text).

4.1.2 The sampling of structure by P- *and* pP-*wave ray paths: hit count*

Information about the sampling of Earth structure in the mantle volume under study can be obtained from mapping

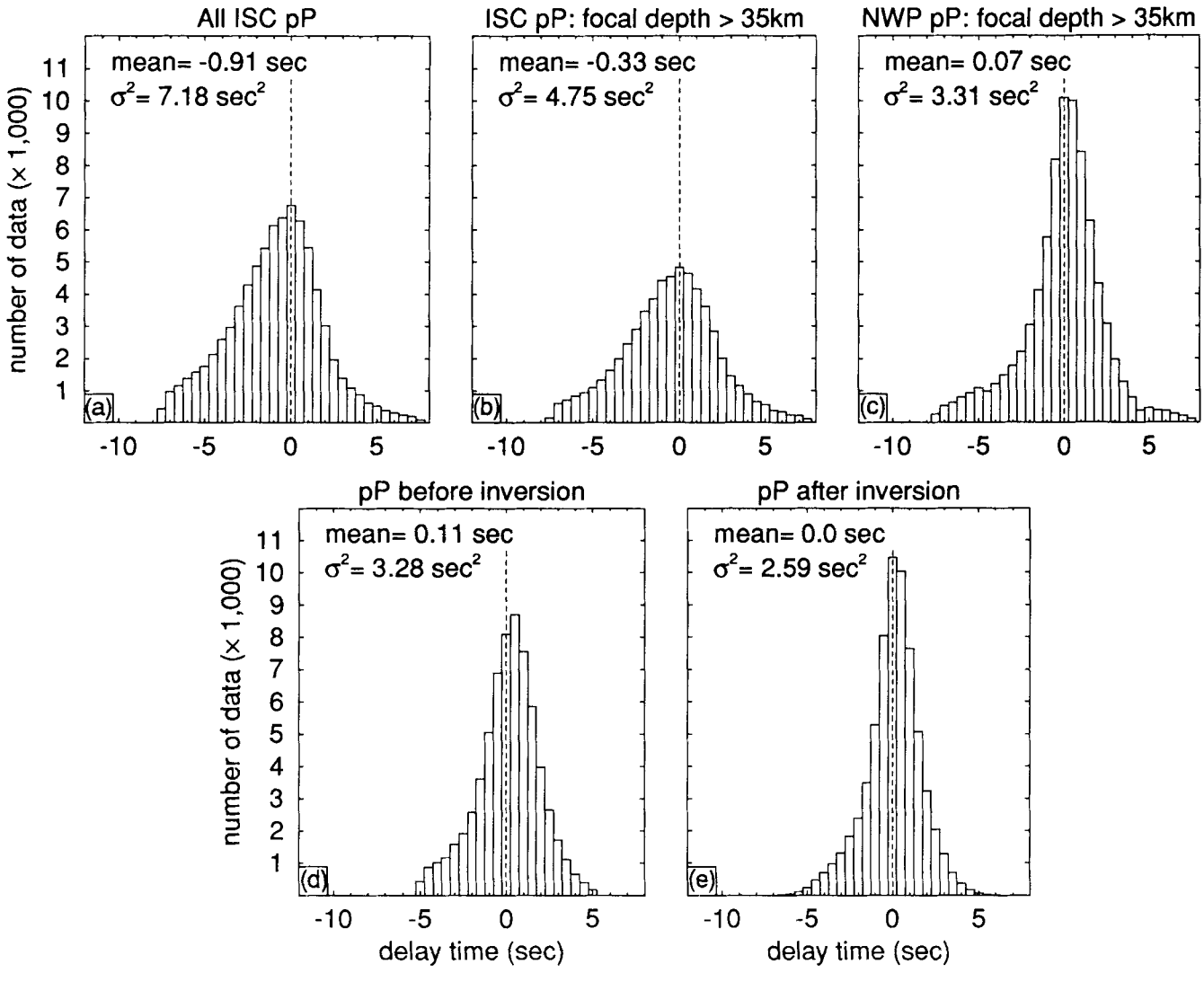

Figure 10. Frequency distributions of *pP* residuals (after Van der Hilst *et al.* 1991). (a) All ISC *pP* delay times from northwest Pacific earthquakes. (b) ISC *pP* data from earthquakes with focal depth exceeding 35 km. (c) New *pP* data after reprocessing the ISC hypocentres (NWP2). (d) *pP* delay times (composite) after clustering procedure which are input to the tomographic inversion. (e) *pP* residuals after inversion (35 iterations).

the number of rays (the hit count) that pass through a particular block of the model depicted in Fig. 2. In Figs 14[1–11](b) and 15[12–19](b) we display the combined hit count of *P*- and *pP*-wave ray paths. The irregular and strongly inhomogeneous sampling by seismic rays is caused both by the uneven distribution of sources (Figs 1b and 13) and receivers (Fig. 6), and by the gradients in the reference velocity-depth profile (Fig. 4).

It is important to realize that the block hit count does not provide information about the ray path directions that are being sampled. There is no direct relationship between hit count and spatial resolution (Spakman & Nolet 1988). Below island arcs, for instance, the hit count is usually high, but slab structure will be poorly resolved if the ray paths used sample the structure from only a limited range of directions (Spakman *et al.* 1989).

Spakman & Nolet (1988) discussed intrinsic damping properties of the LSQR algorithm (also Van der Sluis & Van der Vorst 1987) and the relation between hit count and the amplitudes of the seismic velocity anomalies that were imaged. The least-squares solution converges fast in well-sampled regions within the parameterized mantle volume and the amplitudes of the velocity variation will be biased to zero in poorly sampled mantle regions. This property of the LSQR algorithm is particularly relevant in assessing the effect on resolution of the incorporation of *pP* data (*cf.* Section 4.1.6).

4.1.3 First resolution test: block-anomaly model

To assess the spatial resolution in the tomographic images we performed sensitivity tests (*cf.* Section 2.3; Spakman & Nolet 1988) with both 'block' and 'harmonic' anomaly input models.

The inversion response to a slowness anomaly in a single block provides valuable information about the amplitude recovery of velocity variations, and about the distortion in the shape of the anomaly due to imperfect sampling

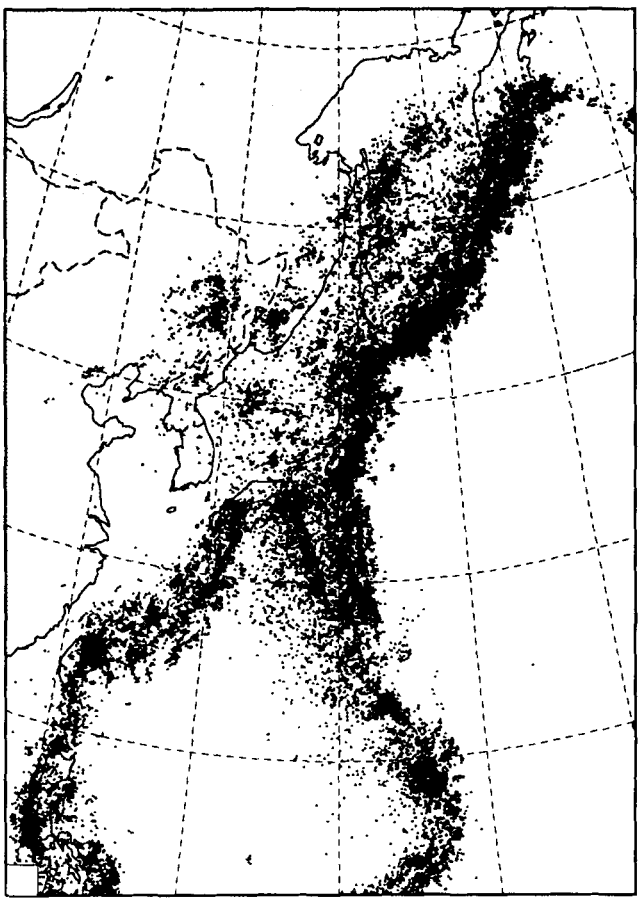

Figure 11. Distribution of pP reflection points.

(Spakman & Nolet 1988; Humphreys & Clayton 1988). Obviously, it is not feasible to compute the impulse response for each of the 48 750 blocks in the model. However, by assigning velocity perturbations only to well-separated blocks, it is possible to approximate the impulse responses in many of the blocks in a single run (Spakman & Nolet 1988).

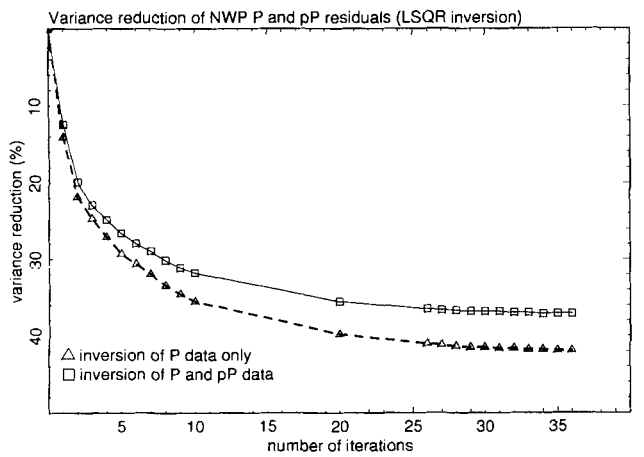

Figure 12. Reduction of residual variance as a function of the number of iterations in the inversion. The curve with open circles depicts the decrease in residual variance when only P-wave data and ray paths are used in the inversion; open squares depict the reduction when pP as well as P data and ray paths are used.

In our application, the input anomalies have amplitudes of 5 per cent relative to the layer iasp91 average (Table 1) and are separated by at least two blocks in the horizontal direction, and by one block in the vertical direction. The tests with this model are useful in assessing the resolution of the short-wavelength variation in seismic velocity. For lithosphere, upper mantle, and transition zone layers, the inversion response to this model is shown in Figs 14[1–11](d).

4.1.4 *Second resolution test: harmonic-anomaly model*

The use of the harmonic model (Spakman & Nolet 1988) serves the purpose of testing the resolution of smooth spatial variation in seismic velocity in the mantle volume under study. The inversion response to the harmonic input model is presented in Figs 14[1–11](e) and 15[12–19](d).

The synthetic model is constructed by the superposition of orthogonal sinusoidal variation in seismic velocity. The input amplitude of the aspherical variation is 5 per cent relative to the iasp91 model. In the horizontal direction, the model anomaly varies with a predominant wavelength of six blocks (approximately 660 km at the surface of the Earth).

4.1.5 *Fit between harmonic input model and inversion response*

The detailed examination of the correlation between the input models and the inversion responses is important. However, it is inconvenient if one wants to get just a quick impression of the overall amplitude recovery, or display the results of the resolution tests by means of arbitrarily selected cross-sections through the block model or to investigate the effect on resolution of the addition of pP-wave ray paths. Therefore, we also display the fit between the harmonic input model and the inversion response to it. The fit, displayed in Figs 14[1–11](c) and 15[12–19](c), is smoothed with a moving average filter over three blocks laterally, and over one layer in depth (*cf.* Spakman & Nolet 1988, p. 177).

4.1.6 *Effects on resolution of the incorporation of* pP*-wave ray paths*

From the distribution of pP reflection points in the northwest Pacific region (Fig. 11) we can expect that the addition of pP-wave ray paths improves the sampling of structure only in specific mantle regions. Because of the properties of the LSQR algorithm (*cf.* Section 4.1.2) this can result in a spatial shift in convergence rate of the inversion algorithm (Van der Hilst & Engdahl 1991, their Fig. 15). The effect of the spatial variation in convergence rate of the inversion algorithm on the resolution of northwest Pacific mantle structure is illustrated in Figs 14[1–11](f), in which we compare the harmonic model fit (*cf.* Section 4.1.5) determined from the combination of P and pP paths (Figs 14[1–11](c)) with that determined from P-wave ray paths only. Negative values indicate that, after 30 iterations, the recovery of the input model obtained with P- and pP-wave ray paths is worse than the recovery obtained with only P-wave ray paths. Positive values indicate mantle regions that benefited directly from the inclusion of pP-wave ray paths. Note that large fluctuations can exist in regions where the absolute value of the fit is small.

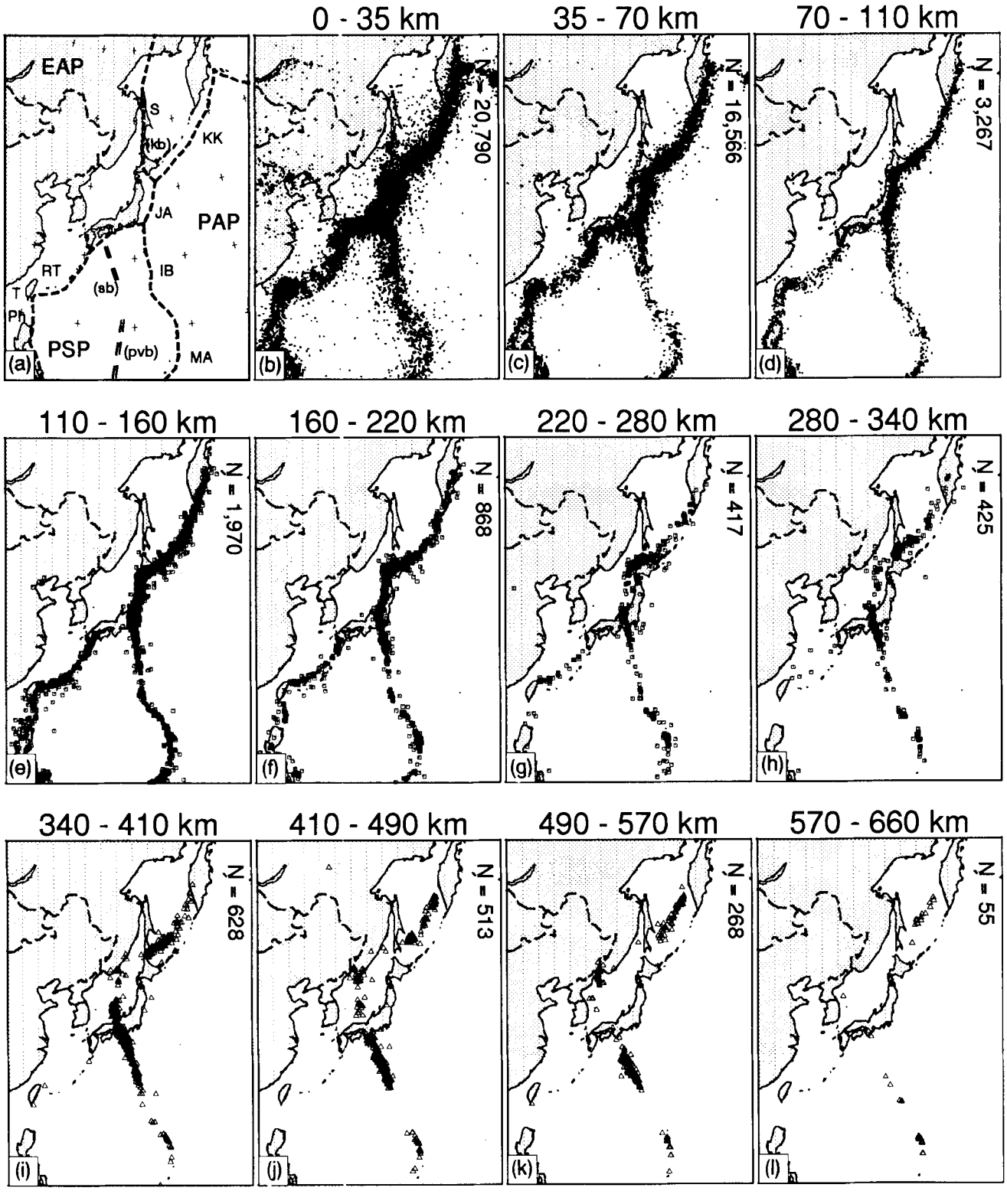

Figure 13. Seismicity within depth intervals by layers of the block model. In (a) the following abbreviations are used: EAP = Eurasian plate, JA = Japan trench, IB = Izu–Bonin trench, kb = Kuril basin, KK = Kuril–Kamchatka trench, MA = Mariana trench, PAP = Pacific plate, Ph = Philippines, PSP = Philippine Sea plate, pvb = Parece Vela basin, RA = Ryukyu trench, S = Sakhalin island, sb = Shikoku basin, T = Taiwan.

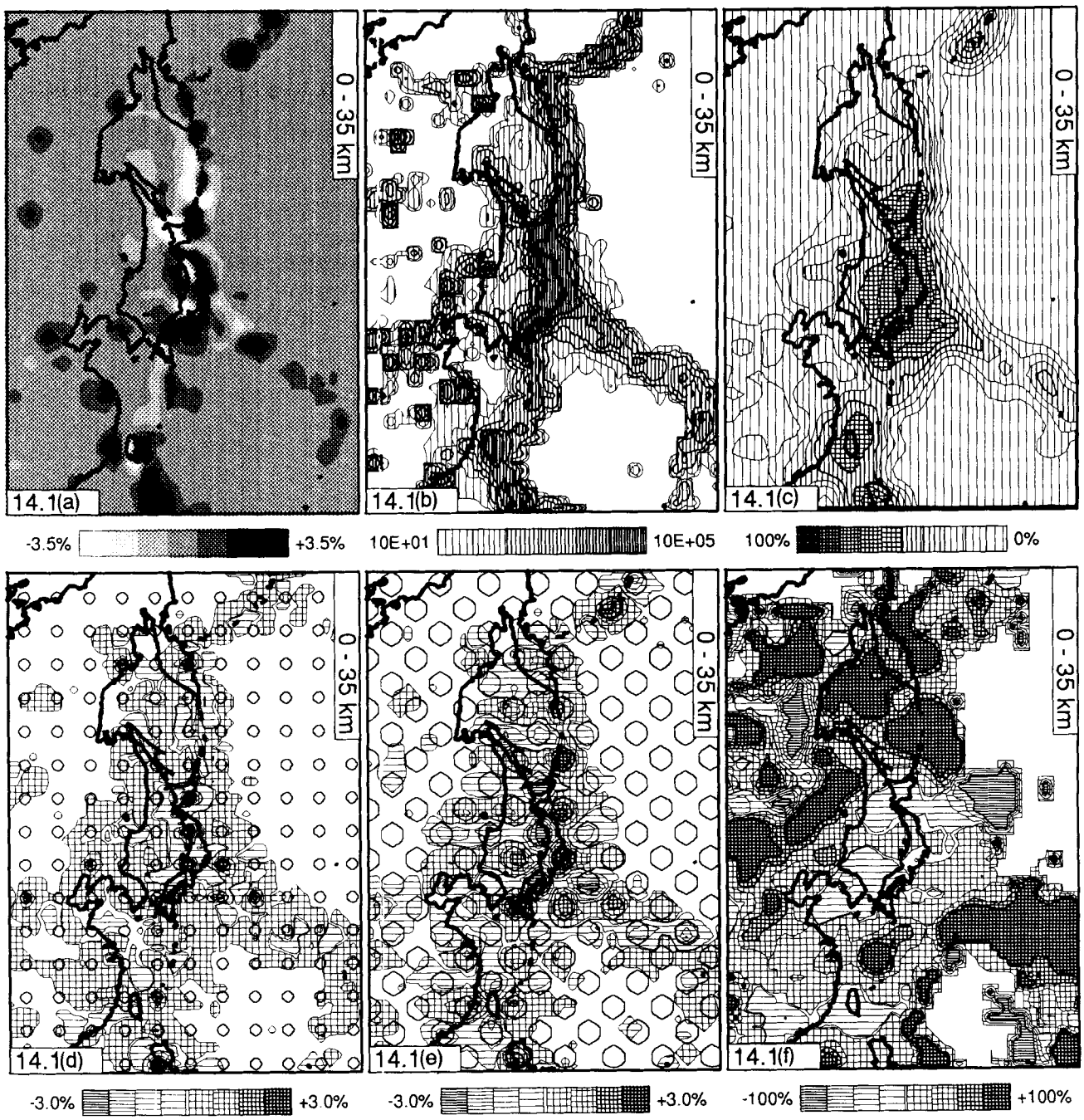

Figure 14. Inversion results for lithosphere, upper mantle, and transition zone layers of the block model (see text Section 4.1 for a detailed explanation). The numbers [1–11] correlate to the layer numbers in Table 1. (a) [1–11] Solution of the inversion for aspherical Earth structure. Velocity perturbations relative to iasp91 are contoured in seven intervals between −3.5 and +3.5 per cent (*cf.* Section 4.1.1). (b) [1–11] Sampling of structure. Number of rays that sample blocks of the cell model (hit count, *cf.* Section 4.1.2). The scale is logarithmic. (c) [1–11] Resolution test. Fit between checker board-type input model and inversion response (*cf.* Section 4.1.5). A value of 0 per cent indicates that the input structure is not resolved. A value of 100 per cent would indicate perfect recovery of input structure. (d) [1–11] Resolution test. Inversion response to the block anomaly model (*cf.* Section 4.1.3). (e) [1–11] Resolution test. Inversion response to the harmonic anomaly model (*cf.* Section 4.1.4). (f) [1–11] Effect on resolution of incorporating *pP*-wave ray paths (*cf.* Section 4.1.6). The values are given with respect to the model fit obtained with *P*-wave ray paths only (*cf.* Section 4.1.5).

4.2 Aspherical mantle structure below northwest Pacific island arcs

We describe only the most striking observations for the crustal and lithospheric layers (Section 4.2.1), the upper mantle depth intervals from 70 to 220 km (4.2.2) and 220 to 410 km (4.2.3), the transition zone (4.2.4), the lower mantle above 1020 km (4.2.5), and the lower mantle between depths of 1020 and 1600 km (4.2.6). Lateral variation of *P*-wave velocity in mantle regions characterized by poor resolution is not discussed.

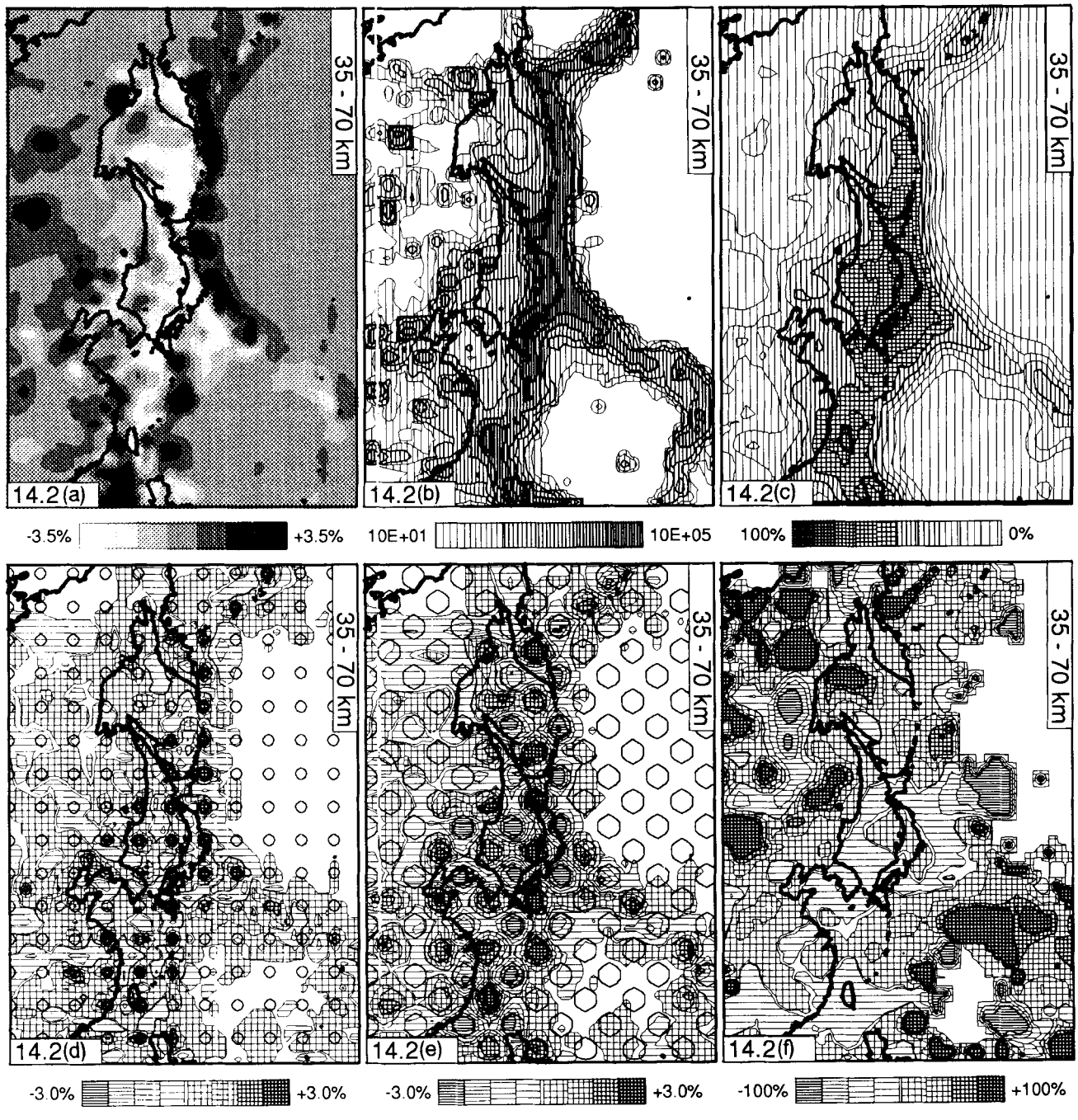

Figure 14. (*Continued.*)

4.2.1 *Depth interval: 0–70 km (layers 1 and 2)*

Sampling of structure. The hit count in the depth interval defined by layers 1 and 2 of the block model is high, but varies rapidly along the island arcs (Figs 14[1–2]b) due to the direct dependence on the locations of sources and receivers. The distribution of the hit count is fairly homogeneous only below Japan. We remark that if only *P*-wave ray paths were considered the hit count would have been near zero in the blocks of Fig. 2 corresponding to the shallow mantle below intraplate regions. The hit count in those regions is primarily due to *pP*-wave ray paths (Fig. 11).

Spatial resolution. The results of the two resolution tests (Figs. 14.1d,e) show that in this depth interval short- and long-wavelength variations in velocity are only resolved below Japan and the Izu Bonin arc, where the sampling of structure is most homogeneous. Fig. 14.1(e) indicates that in a large region the sign of the input anomaly [i.e. fast (+) or slow (−)] is resolved, but that the resolution degrades towards the Marianas and the northern part of the

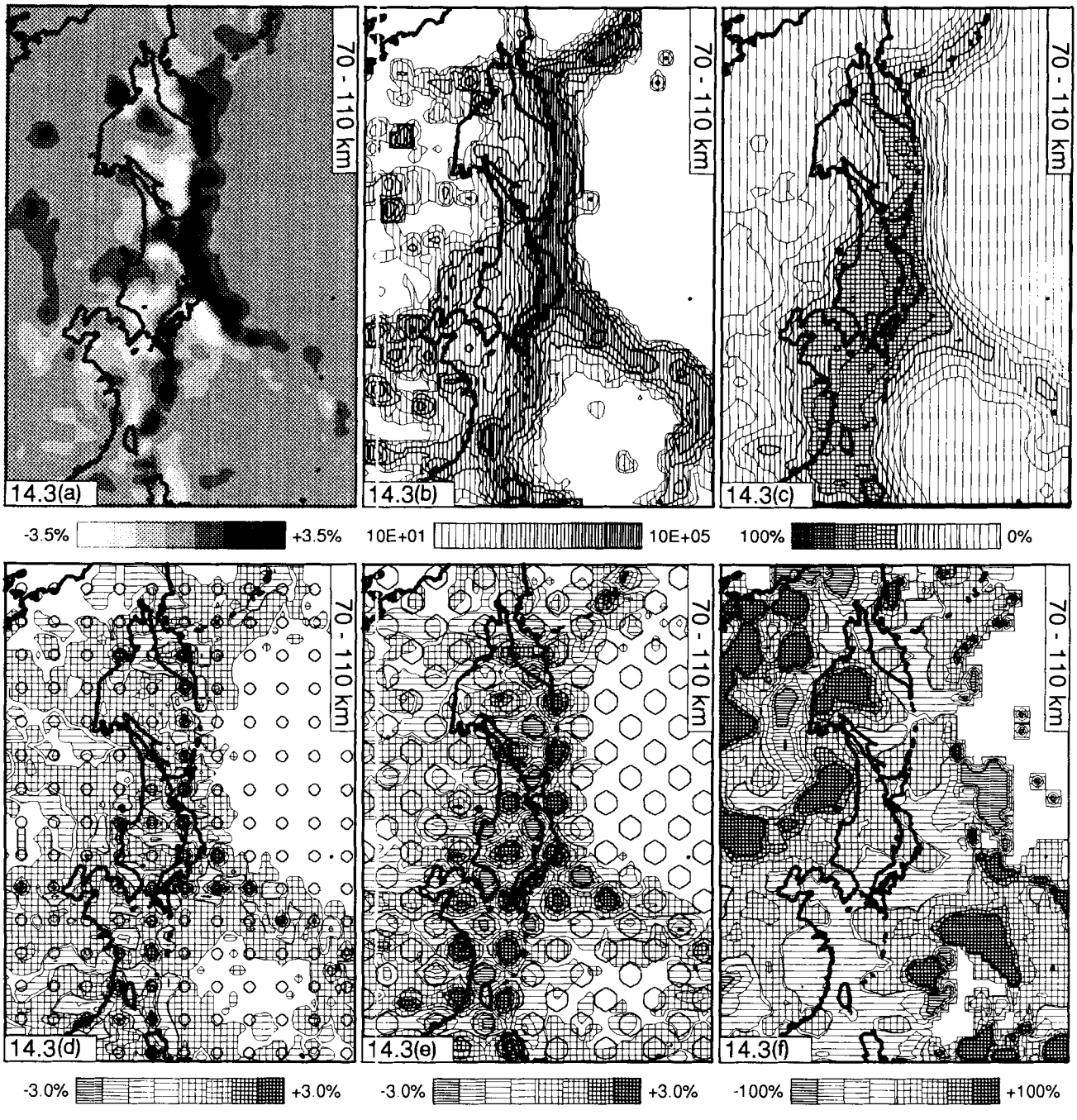

Figure 14. (*Continued.*)

Kuril–Kamchatka arc (see also Figs 14.[1–2]c). For the crustal layer, up to 80 per cent of the input model is recovered in the region below Japan (Fig. 14.1c). The model fit is indicative of reasonable resolution of shallow structure below the convergent margins near Taiwan and the Philippines, and along the Aleutian arc.

Comparison of Figs 14.1(c), (d) and (e) with Figs 14.2(c), (d) and (e) shows that the resolution at subcrustal depths is significantly better than in the shallowest layer. This is a result of the more effective sampling by the ray paths involved (Fig. 14.2b). In the second layer, the resolution of small-scale structure is good below the southern Kuril and Japan arc, reasonable below Izu Bonin, Ryukyu, and the Philippines, but poor below the Mariana arc. Structures with longer wavelengths are well resolved below most regions of our interest. The resolution decreases from the Izu Bonin arc southward, although the sign of the anomalies is resolved below the Mariana arc.

Figures 14[1–2](f) demonstrate that in many regions the resolution of shallow mantle structure improved considerably by the incorporation of *pP*-wave ray paths. The resolution improved, in particular, below intraplate regions (Sea of Okhotsk, continental Asia) and below island arcs where only a few stations are located (Fig. 6). The

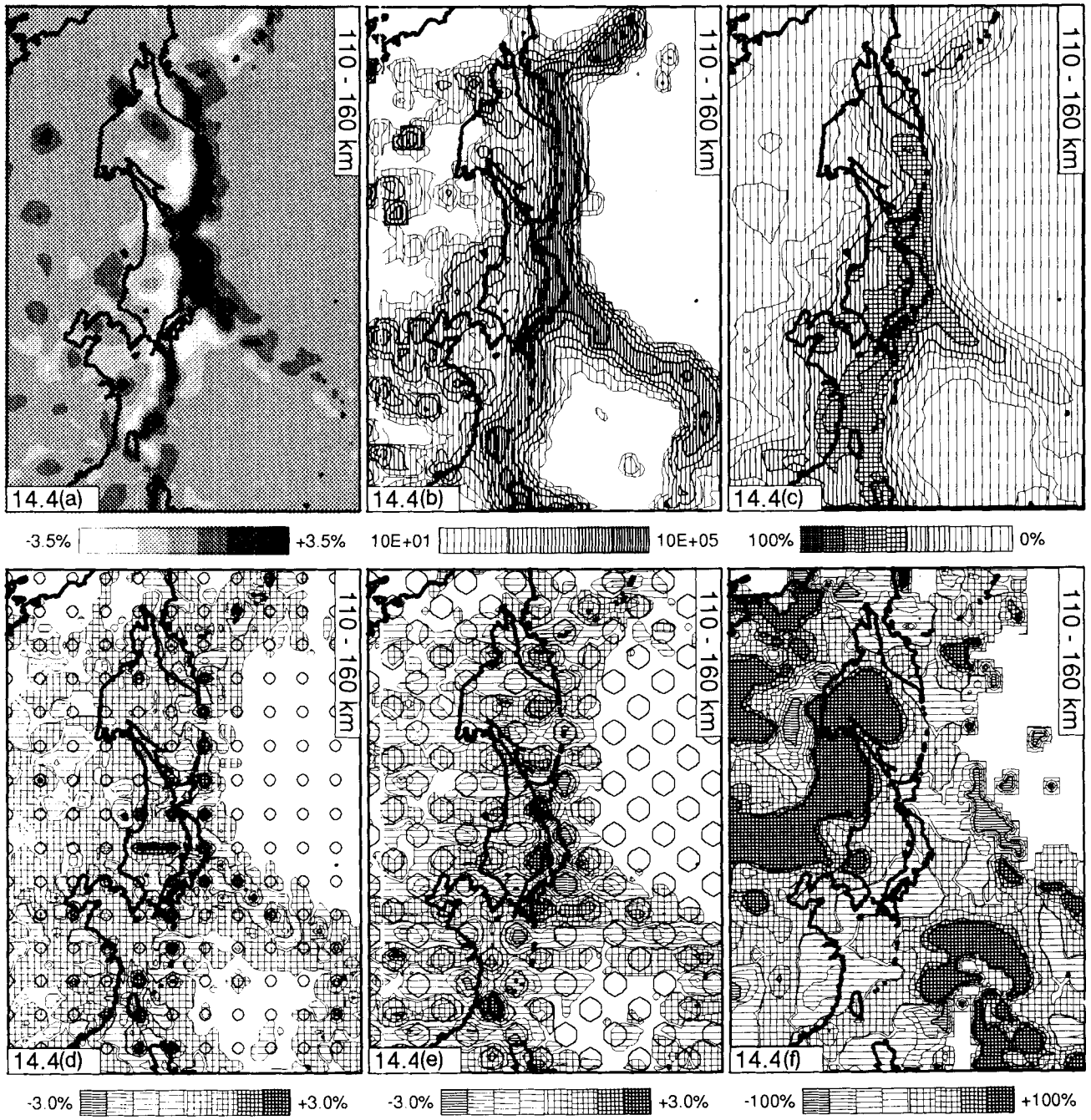

Figure 14. (*Continued.*)

improvement in the central region—near Japan—is remarkable, for the amplitude recovery of the input model is very high. Note the improvement of resolution—often of the order of 100 per cent—is not always relevant, because the absolute fit is low in geographical regions below which structure is not effectively sampled by the *P*-wave paths used in the inversions (Figs 14[1–2]c).

Aspherical Earth structure. In the upper 70 km, the aspherical variation in seismic velocity is irregular (Figs 14[1–2]a) as a result of the inhomogeneous sampling by the ray paths used. For depths between 35 and 70 km the velocity variations imaged are laterally more coherent (Fig. 14.2a). A characteristic pattern of fast and slow mantle regions below convergent margins becomes visible; from the Aleutians to Izu Bonin the mantle region below the island arcs is marked by higher-than average *P*-wave velocities. High *P*-wave velocities are also imaged below the Philippine Sea side of the Ryukyu arc. Below the Mariana islands *P*-wave velocities are imaged to be high but the amplitude of the perturbations are significantly lower than elsewhere.

Mantle regions below the marginal basins are marked by slow *P*-wave propagation. The zone of low *P*-wave velocities west of the Izu Bonin arc is not continuous to the

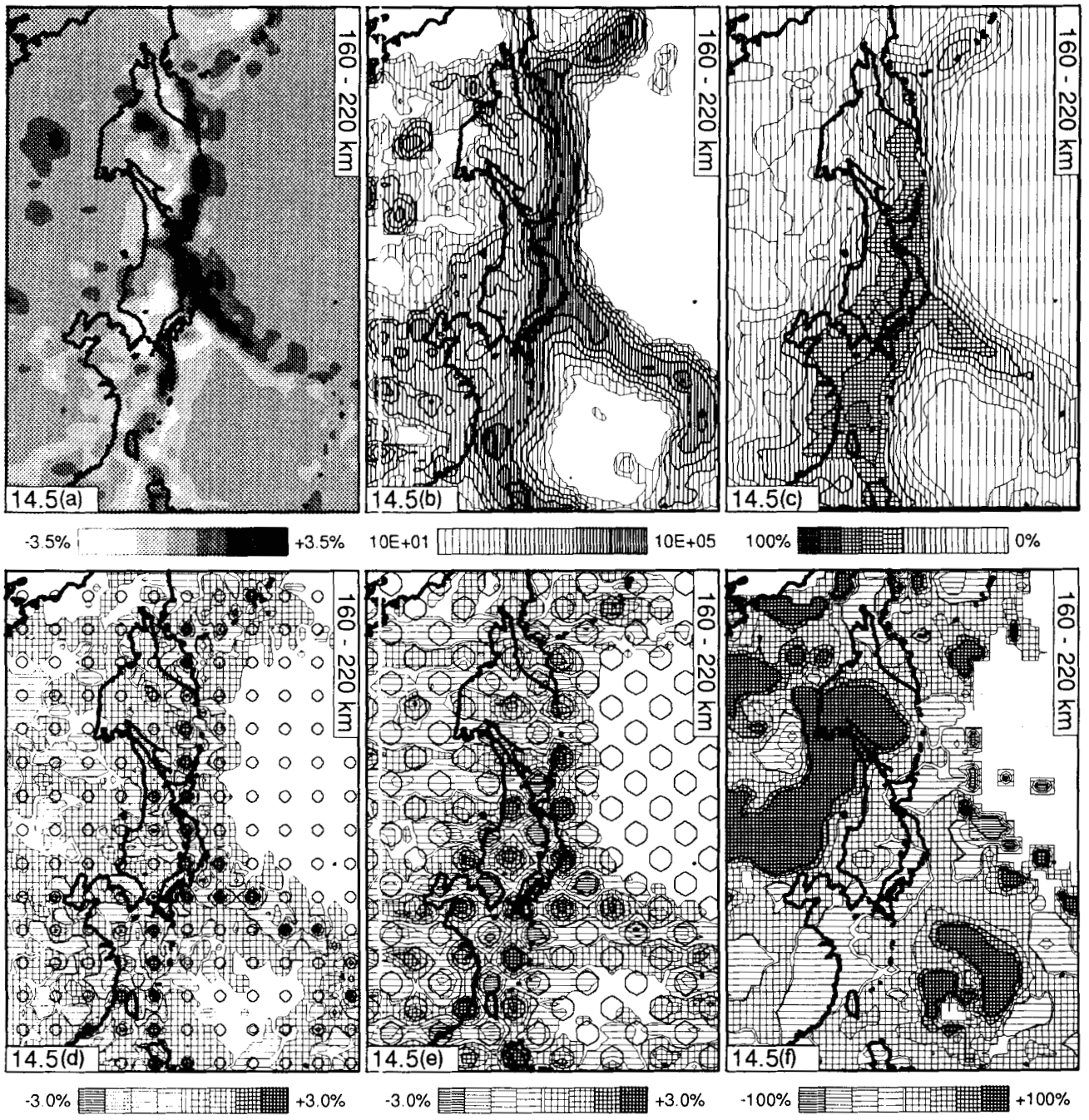

Figure 14. (*Continued.*)

Mariana region. Fig. 14.2(c) reveals that structure is not well resolved below the back-arc area of the Mariana arc, and the drop in amplitude from the Izu Bonin southwards is probably overestimated. The *P*-wave velocity below the southern part of the Sea of Okhotsk—above the Kuril seismic zone—is imaged to be up to 6 per cent lower than iasp91. See also last paragraphs of Section 5.2 below.

4.2.2 *Depth interval: 70–220 km (layers 3, 4 and 5)*

Sampling of structure. Ray paths of *P* waves recorded at epicentral distances between approximately 10° and 16° bottom in this depth interval. Figs 14[3–5](b) do not reveal substantial differences in sampling over these three depth levels, although the quality of sampling improves with increasing depth, particularly below intraplate regions.

Spatial resolution. The response to the harmonic model (Figs 14[3–5]e) shows that the recovery of the smooth variation in seismic structure is good below the Kuril, Japan, Izu Bonin and Ryukyu/Philippine arcs, but poor below the Mariana and Aleutian arcs. Small-scale structures are well resolved below the southern part of the Kuril arc, and below the Japan, Izu Bonin and Ryukyu island arcs. The response

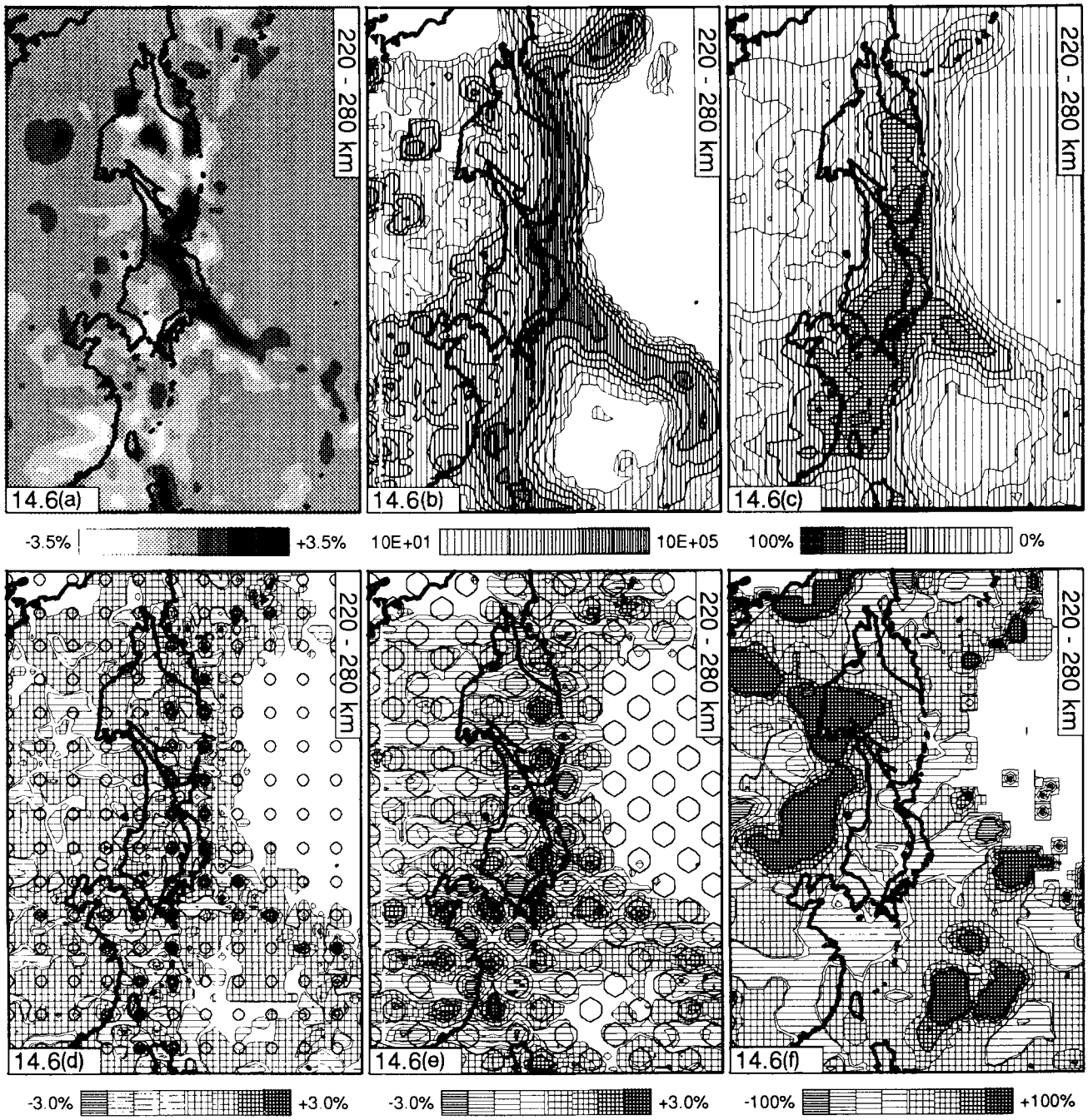

Figure 14. (*Continued.*)

to the block anomaly model (Figs 14[3–5]d) shows that the locations of the input anomalies are reasonably well recovered below the Mariana arc, but that the recovery of the amplitude is poor. The spurious anomalies present between locations in the input model (Figs 14[4–5]d) are due to 'leaking' from adjacent layers, which signals lack of vertical resolution over this depth range in the Mariana region.

Figures 14[3–5](c) show that the model fit is very good below most island arcs except for the Aleutians and Marianas. In the depth interval between 70 and 220 km, the resolution generally improved with the incorporation of the *pP*-wave ray paths (Figs 14[3–5]f), particularly below intraplate regions and below the Izu Bonin and Mariana island arcs. At depths between 110 and 160 km (layer 4) the model fit is less than in the adjacent depth intervals. Few ray paths bottom between 110 and 160 km in depth due to variation of *P*-wave velocity in the iasp91 reference model. The effect on the model fit of incorporating *pP*-wave ray paths is, therefore, larger in that depth range (Fig. 14.4f) than in the shallower layer (Fig. 14.3f) (see last paragraph of Section 2.2 for discussion).

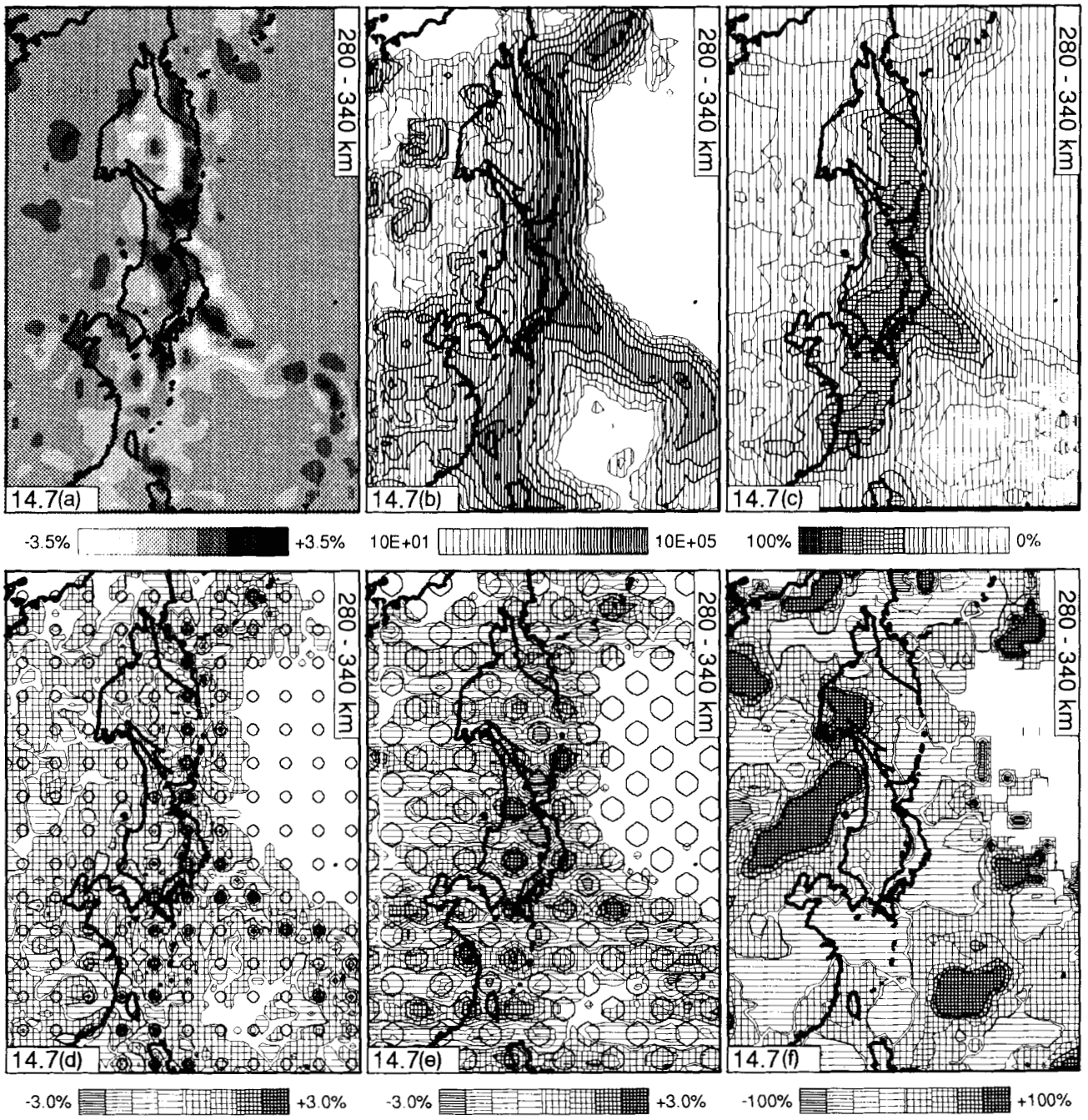

Figure 14. (*Continued.*)

Aspherical Earth structure. Between 70 and 220 km the images of aspherical structure are predominated by a zone of fast wave propagation that is continuous along the seismic zones (Figs 13[c–e]) below the Kuril, Japan, and Izu Bonin island arcs (Figs 14[3–5]a). The lateral variation in velocity along the Izu Bonin and Mariana arcs is similar to those described for the shallower depths (Fig. 14.2a): high *P*-wave velocities are imaged below the Izu Bonin arc, but there is no indication for similar fast *P*-wave propagation further to the southeast. As mentioned above, the drop in amplitude coincides with the degradation of resolution (Figs 14[3–5]c). The images indicate fast wave propagation below the Ryukyu arc, although the amplitudes of the velocity variation is small between 170 and 220 km (Fig. 14.5a).

Below the marginal basins, in particular below the southern part of the Kuril arc and the Shikoku basin west of the Izu Bonin trench, the images depict *P*-wave velocities up to 5 per cent slower (Fig. 14.3a) than iasp91 at the corresponding depths. See also last paragraphs of Section 5.2 below.

Lateral changes in seismic velocity are visible below the southern Japan area where both the hit count (Figs 14[3–5]b) and the mode fit (Figs 14[3–5]c) are fairly homogeneous. In contrast, there are similarities between the

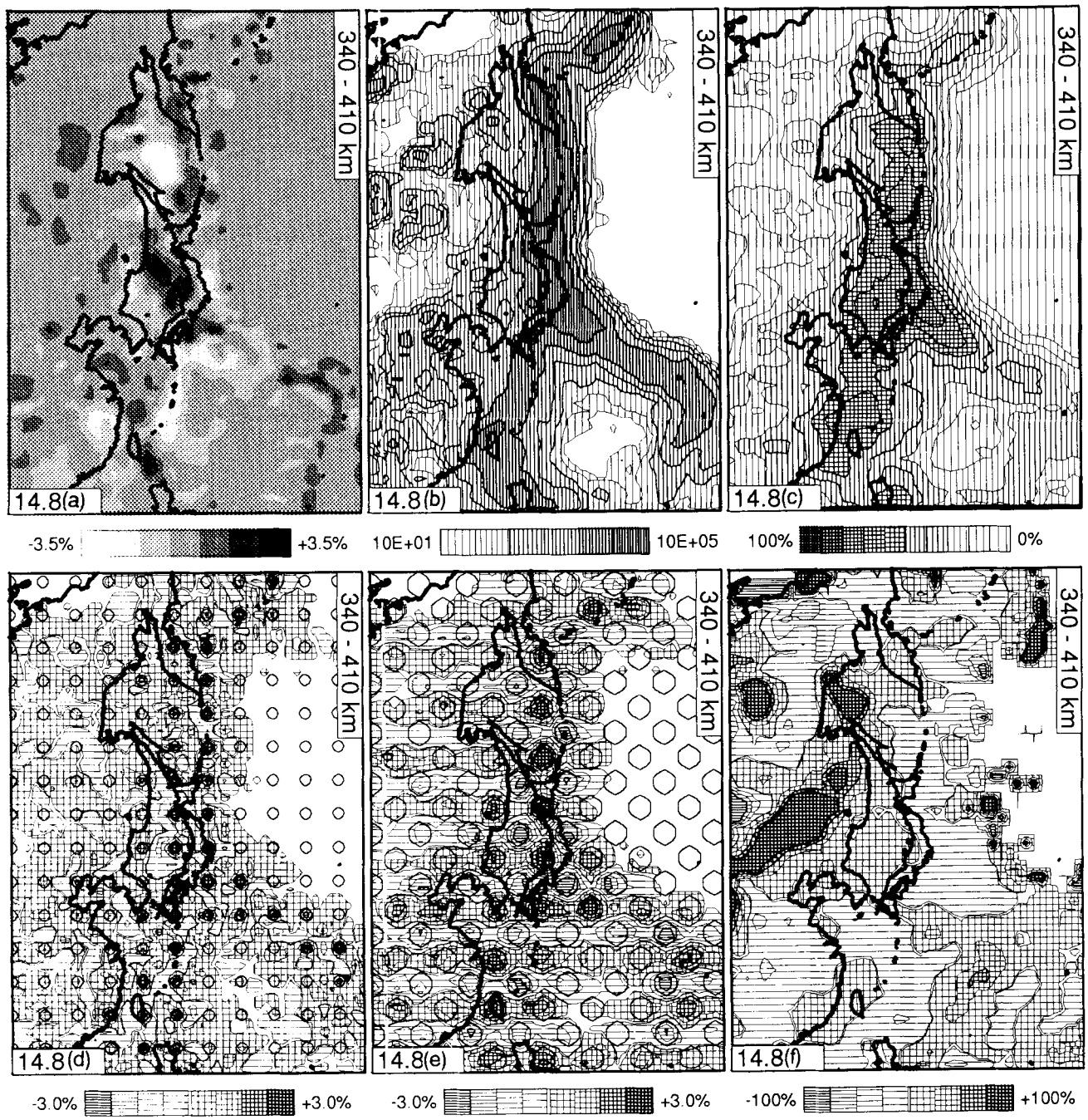

Figure 14. (*Continued.*)

variation in seismic velocity, hit count, and model fit along the strike of the Izu Bonin and Mariana arcs (Figs 14[3–5]a, b and c) and we must thus be cautious in interpreting aspherical variation in seismic velocity in this depth range. The lateral variation in velocity is, however, more abrupt than the hit count (Figs 14[3–5]b) and model fit (Figs 14[3–5]c). This suggests that the location of the perturbations is real, but that the drop in amplitude of the velocity variation relative to iasp91—from the northern Izu Bonin southward—is probably overestimated.

4.2.3 Depth interval: 220–410 km (layers 6, 7 and 8)

Sampling of structure. There is a further improvement in the sampling of Earth structure with increasing depth. The ray paths associated with the first-arriving *P* waves recorded at epicentral distances between 16° and 20° bottom in the depth range between 220 and 410 km. Because of the presence of the '410 km' discontinuity in the reference model (Fig. 3) no first-arriving *P* waves bottom between about 300 and 410 km. The sampling in this depth interval is

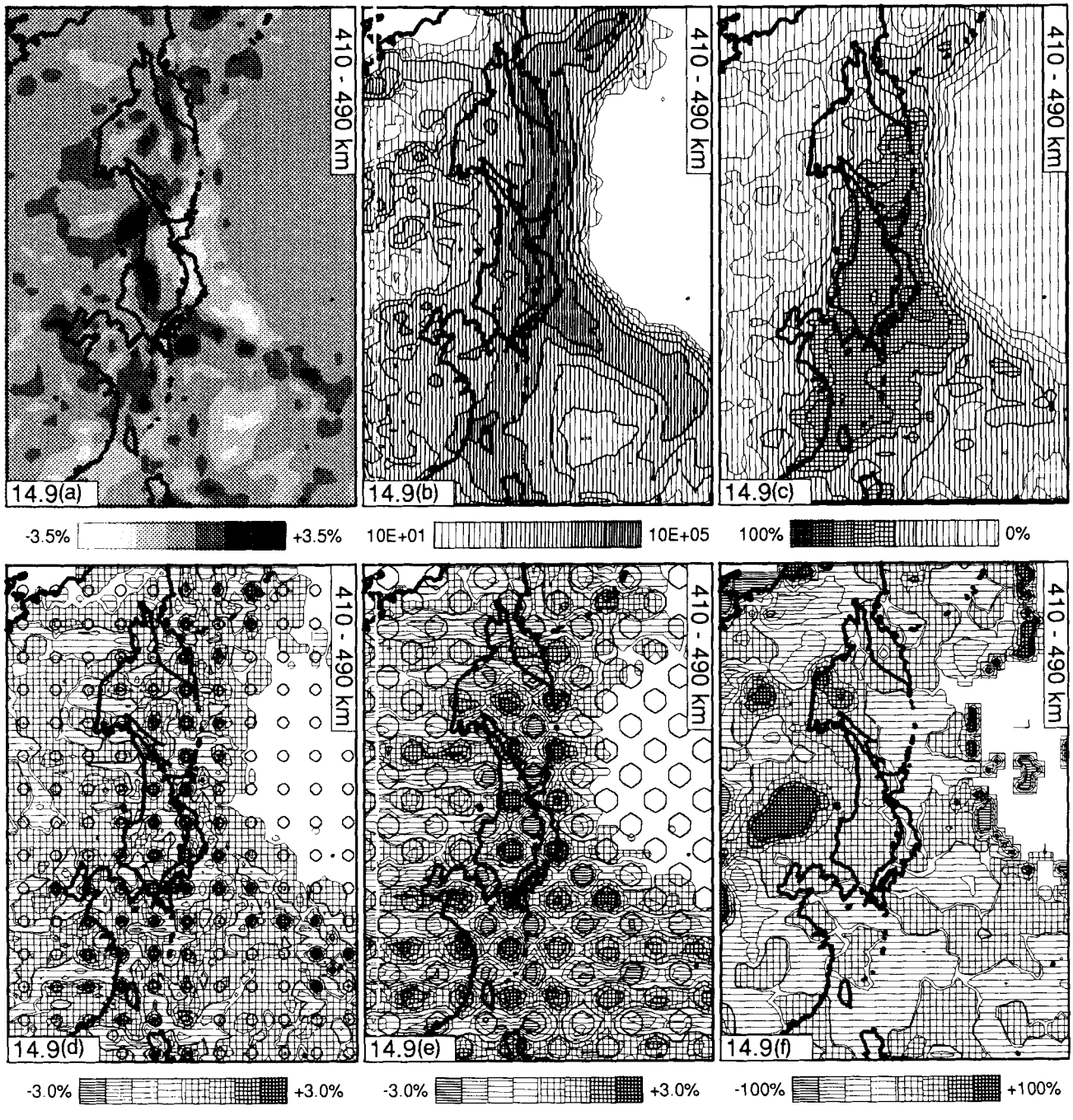

Figure 14. (*Continued.*)

dominated by ray paths of *P*-waves with small ray parameters and by *pP*-wave ray paths (*cf.* Section 2.2.2).

Spatial resolution. The area in which the resolution is good also becomes larger. This is true, in particular, for the resolution of structure with larger wavelengths, as can be inferred from Figs 14[6–8](c and e). Below the central and southern Kurils, Japan, Izu Bonin, and the northwestern part of the Philipine Sea plate, both the locations and the amplitudes of input anomalies are well resolved (Figs 14[6–8] c and e). Figs 14[6–8](d) show that the resolution of small-scale structure is good below the Kuril arc, below Japan and the northern part of the Philippine Sea plate. The presence of spurious anomalies at the locations of the input anomalies of the adjacent layers (Fig. 14.6d) indicates that the vertical resolution is probably poor below Kamchatka, the southern part of the Izu Bonin arc, and below the Mariana arc. At depths between 220 and 410 km, the resolution of mantle structure of all wavelengths is poor below the Aleutian arc, continental Asia and the central part of the Philippine Sea plate.

As the sampling by *P*-wave ray paths becomes more

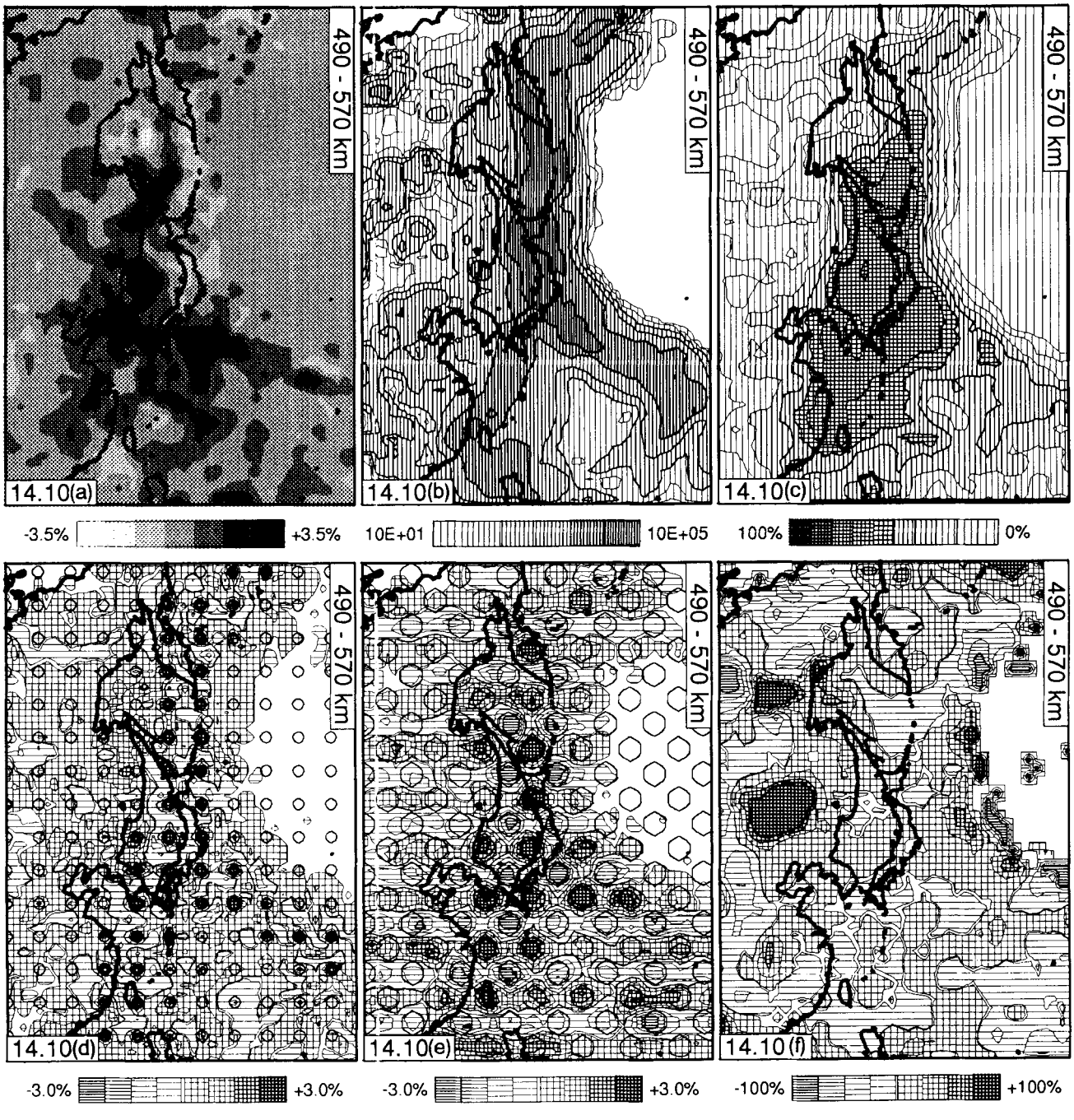

Figure 14. (*Continued.*)

homogeneous with increasing depth, the effect of pP-wave ray paths on the resolution reduces gradually (Figs 14[6–8]f).

Aspherical Earth structure. The lateral coherency of structure between 70 and 220 in depth breaks down between 220 and 410 km (Figs 14[6–8a). Below the Kuril are the sampling of structure and the model fit is fairly homogeneous (Figs 14[6–8]b and c), but the image of the high-velocity zone becomes laterally discontinuous. Below the central part of the Kuril arc, the lateral distance between the high-velocity zone and the arc remains small which indicates a steeply dipping slab. Towards the south, the lateral distance between the trench and the high-velocity zone increases. This is indicative of a shallower dip of the slab below the southern part of the Sea of Okhotsk, which is in agreement with the pattern of seismicity (Figs 13[g–i]).

Below the Izu Bonin arc, the amplitude of P-wave velocity anomalies decreases, whereas high P-wave velocities are now imaged below the Mariana arc. In the mantle region between the northern Izu Bonin and Mariana arcs, the P-wave velocities imaged do not differ significantly from the iasp91 reference model. The drop in amplitude relative to the reference model of the velocity anomalies between

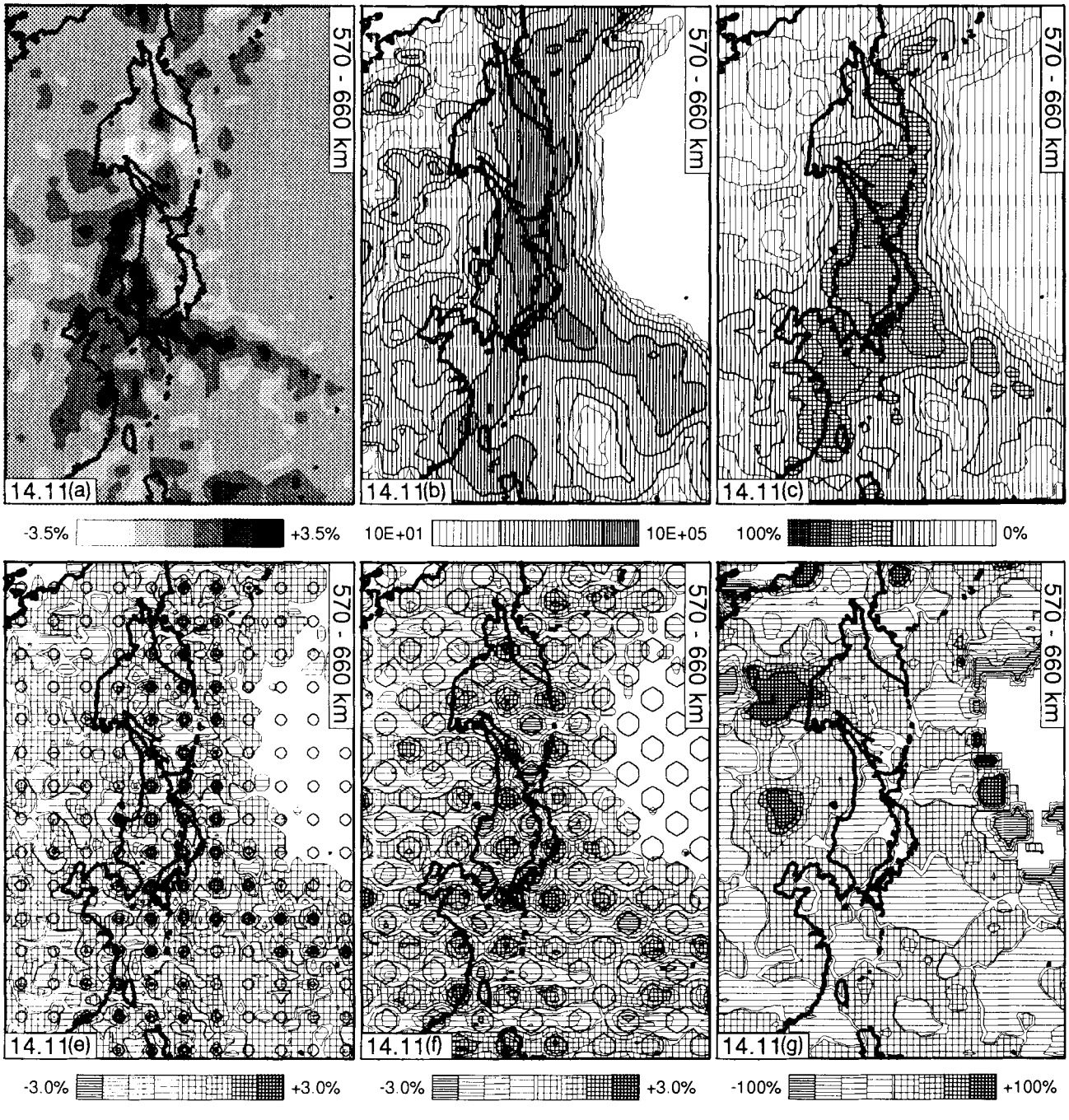

Figure 14. (*Continued.*)

the Izu Bonin and Mariana arcs coincides with changes in hit court (Figs 14[6–8]b) and model fit (Figs 14[6–8]c). Thus, interpretations about the lateral transition of the slab below the Izu Bonin arc to the structure below the Mariana arc from the tomographic images are not conclusive.

Back-arc mantle regions are marked by low *P*-wave velocities even at relatively large depths, although the amplitude of the anomalies is small.

4.2.4 *Depth interval: 410–660 km (layers 9, 10 and 11)*

Sampling of structure. Owing to the effect of the '660 km' discontinuity the number of *P*- and *pP*-wave ray paths drops just above 660 km, in particular in regions outside the seismic zones (*cf.* Section 2.2.1). Compare, for instance, the sampling of structure below the Philippine Sea plate in the depth interval between 570 and 660 km (Fig. 14.11b) to that of the depth interval; between 490 and 570 km (Fig. 14.10b) and between 660 and 750 km (Fig. 15.12b).

Spatial resolution. Figures 14[9–11](c) and (e) show that in most regions the resolution of smoothly varying structure in the transition zone is good. Transition-zone structure is moderately well resolved below the central part of the Philippine Sea plate, but unresolved below continental Asia and the Pacific ocean. The amplitudes in the harmonic

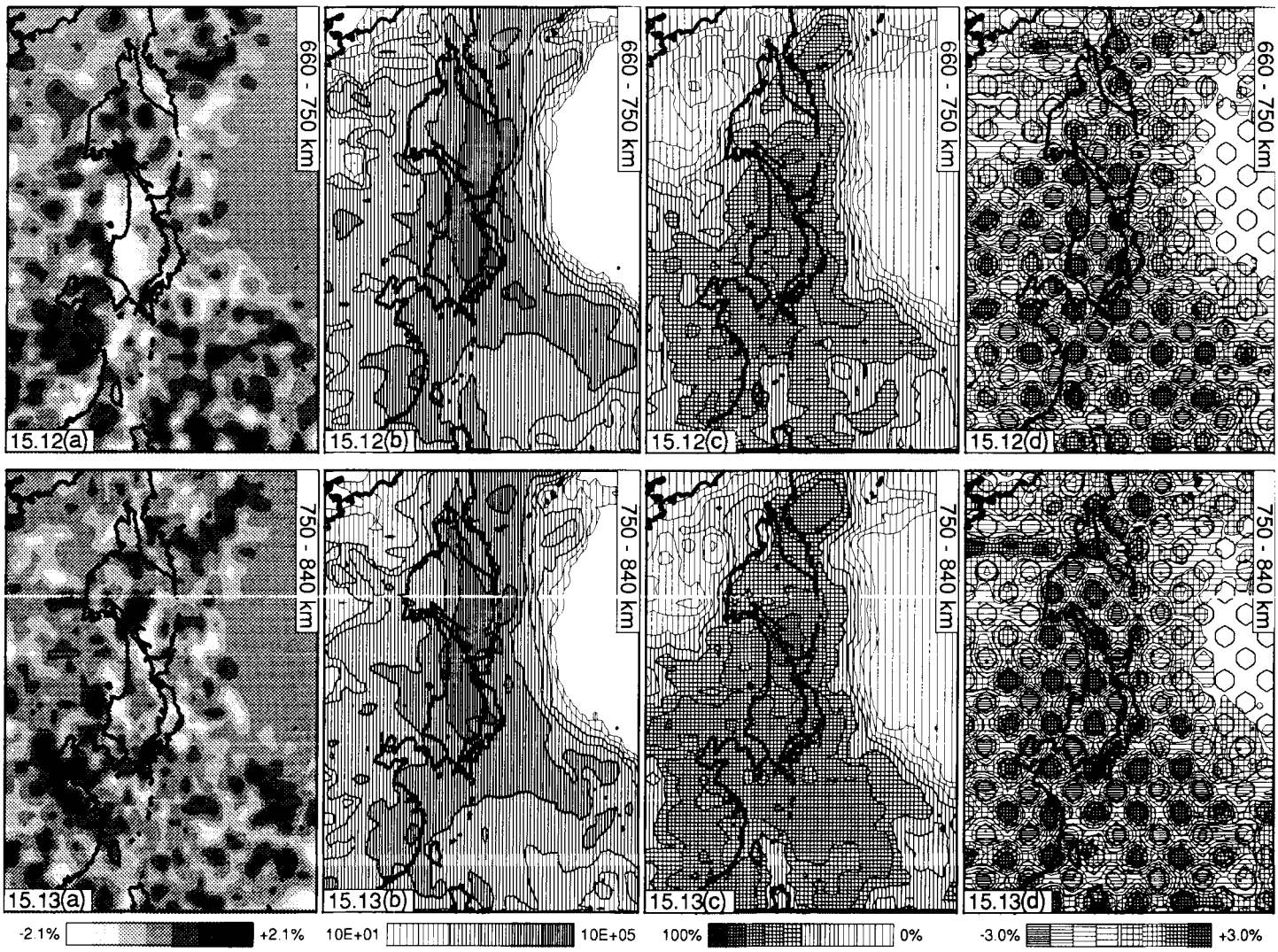

Figure 15. Inversion results for the lower mantle layers of the block model (see text Section 4.1 for a detailed explanation). The numbers [12–19] correlate to the layer numbers in Table 1. (a) [12–19] Solution of the inversion for aspherical Earth structure. Velocity perturbations relative to iasp91 are contoured in seven intervals between −2.1 and +2.1 per cent (*cf.* Section 4.1.1). (b) [12–19] Sampling of structure. Number of rays that sample blocks of the cell model (hit count, *cf.* Section 4.1.2). The scale is logarithmic. (d) [12–19] Resolution test. Inversion response to the harmonic anomaly model (*cf.* Section 4.1.4). (c) [12–19] Resolution test. Fit between checker board-type input model and inversion response (*cf.* Section 4.1.5)

anomaly model are not well resolved (Figs 14[9–11]e) below the central and southeastern (Mariana) part of the Philippine Sea plate. Small-scale structure is not resolved (Figs 14[9-11]d) below continental Asia, the Pacific ocean, the central Part of the Philippine Sea, and below the Mariana and Aleutian island arcs. The vertical resolution is not good below the southeastern part of the Philippine Sea plate.

Aspherical Earth structure. The images reveal high *P*-wave velocities in a narrow zone below Kamchatka and the Sea of Okhotsk, although there is substantial lateral variation in the amplitudes of the velocity anomalies (Figs 14[9–11]a). Northeast of Sakhalin Island the zone of high *P*-wave velocity remains approximately parallel to the Kuril island arc. Further southwest the strike of the slab-like high-velocity feature changes to WSW–ENE and the lateral distance to the trench increases significantly. In the transition zone below the northern part of the Sea of Japan the WSW–ENE striking high velocity is continuous with depth. Northwest of Japan, the strike of the high-velocity zone changes and below the Sea of Japan the strike is NNE–SSW. In the depth interval between 490 and 660 km, the apparent width of the high-velocity structure increases sharply below the Sea of Japan and below the northern part of the Philippine Sea, where the spatial resolution is good. More importantly, the western edge of the high-velocity region does not coincide with variations in hit count and is well resolved (Figs 14.10a, b, c and e). The southern boundary, however, coincides with a rapid drop in the number of *P*- and *pP*-wave ray paths sampling that region and with a reduction in resolution (Figs 14.10c and e).

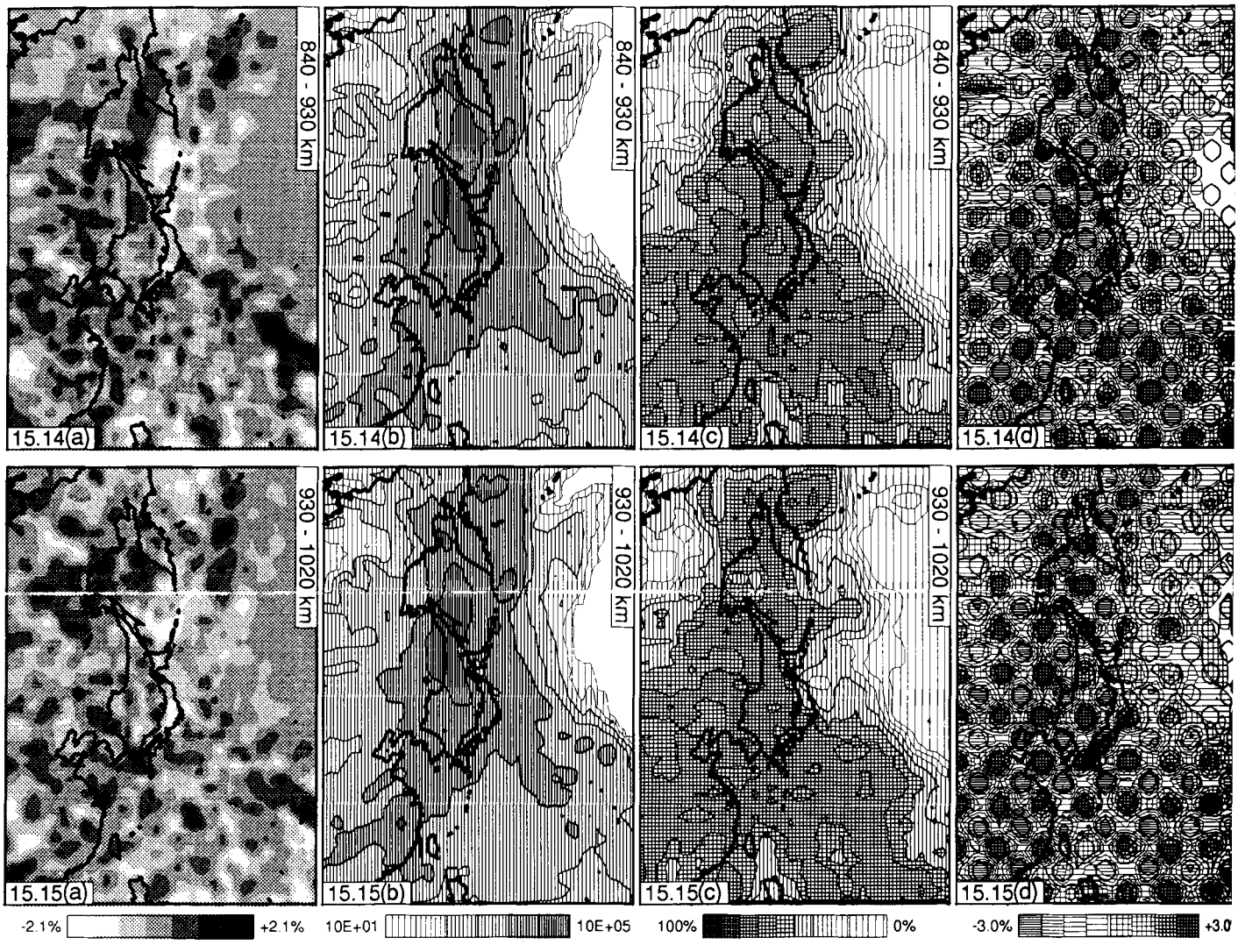

Figure 15. (*Continued.*)

Below the Mariana arc the shape of the high *P*-wave velocity zone does not vary much with depth, indicating that the orientation of the high-velocity slab does not change significantly. Unfortunately, the transition between the wide high-velocity structure below the northern part of the Phillipine sea to the narrow zone below the Mariana arc is not well resolved, particularly in the depth range just above the '660 km' discontinuity (see above). Directly below the arc, the lateral variation in *P*-wave velocity between the Izu Bonin and Mariana arcs is well resolved.

4.2.5 *Depth interval: 660–1020 km (layers 12 to 15)*

Sampling of structure. Ray paths of *P* and *pP* waves travelling to stations at epicentral distances between 25° and 43° bottom in the lower mantle between 660 and 1020 km in depth, and are not significantly influenced by upper mantle discontinuities. The sampling of structure by *P*- and *pP*-wave ray paths is homogeneous below the central part of the region under study (Figs 15[12–15]b). In Fig. 15.15(b) the group of waves travelling to distant stations in North America begins to separate from the waves travelling to stations in Europe.

Spatial resolution. Results of the synthetic tests show that the resolution of smooth lateral changes in *P*-wave velocity is resolved very well in most areas (Figs 15[12–15]c and d). Below the Pacific ocean and below continental Asia the resolution is poor.

Aspherical Earth structure. The imaged variation in lower mantle *P*-wave velocity is markedly different than in the upper mantle and transition zone. A comparison of Fig. 14.11(a) with 15.12(a) shows that the laterally coherent pattern of high *P*-wave velocities is absent in the lower mantle. The high seismic velocities imaged in the transition zone below the Sea of Japan and the northern part of the Philippine sea are absent in the upper 400 km of the lower mantle. In contrast, substantially slower wave propagation is imaged in these regions just below the '660 km' discontinuity (*cf.* Section 5.2 for possible explanation). Below the northern part of the Sea of Okhotsk and below the Mariana

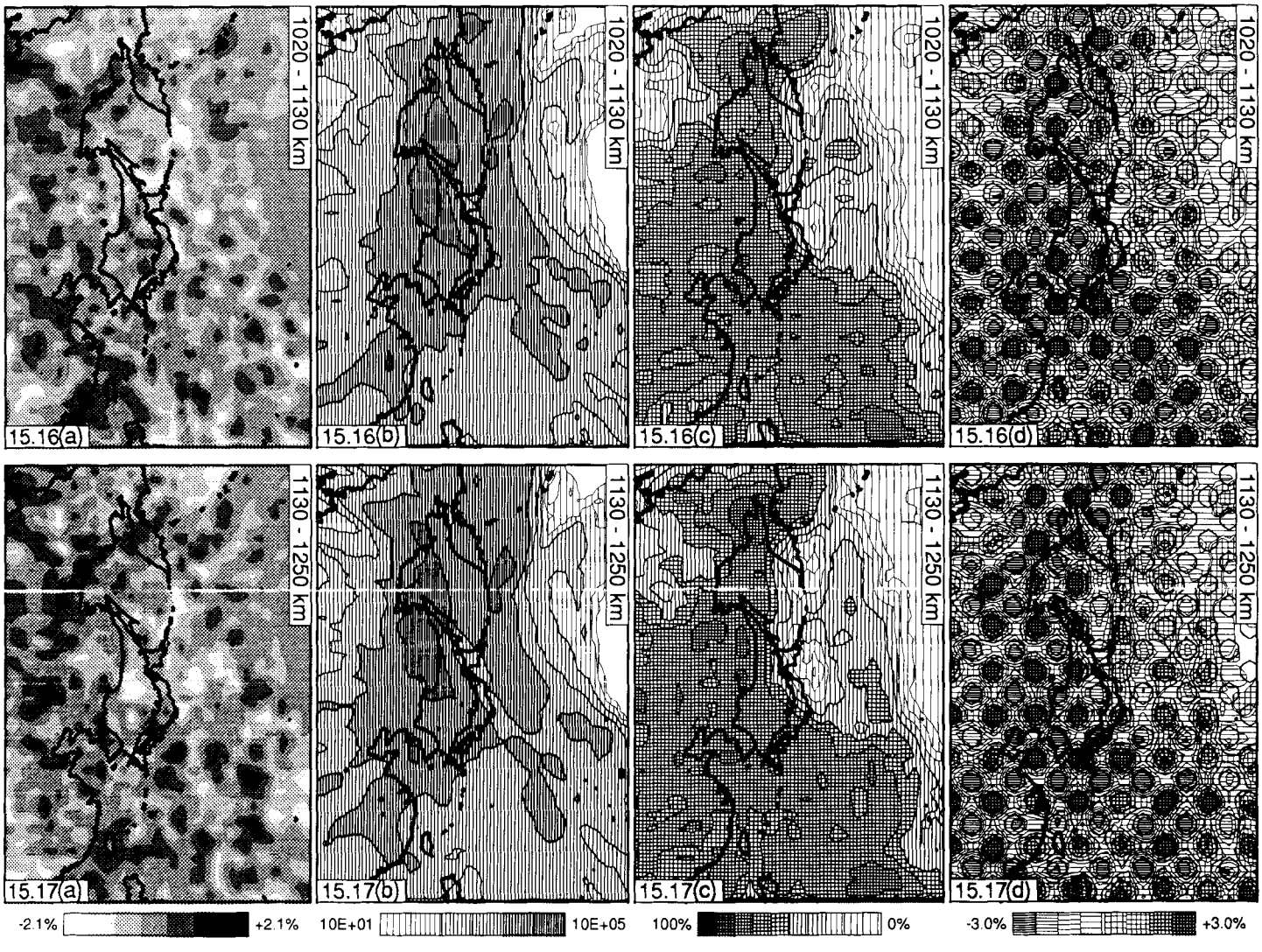

Figure 15. (*Continued.*)

arc, however, the slab-like zones of high *P*-wave velocities imaged in the transition zone are also present in the lower mantle (Figs 15[13–15]a). We note that, with the possible exception of Fig. 15.14(a), they do not stand out above the noise level and although they form structures that are continuous in depth (see the cross sections in NWP1) interpretation in terms of slab structure is somewhat subjective.

4.2.6 Depth interval: 1020–1600 km (layers 16 to 19)

Sampling of structure. Lower mantle structure in the depth interval between 1020 and 1600 km is sampled by *P* and *pP* waves recorded at stations at epicentral distances larger than about 43°. For our study, the majority of these stations are located in Europe and North America. The predominance of *P*- and *pP*-wave ray paths to stations in these two geographical regions is visible in Figs 15[16–19](b). As a consequence of the spatial separation between ray paths to stations in either Europe or North America, lower mantle structure below northeastern Japan is not well sampled.

Spatial resolution. In most areas, the resolution of lower mantle structure between 1000 and 1600 km is good (Figs 15[16–19]d), but the characteristics of the sampling of lower mantle structure (see above) are reflected in the resolution and with increasing depth the resolution decreases below northeastern Japan (Figs 15[16–19]c and d).

Aspherical Earth structure. In general, the images of aspherical variation in *P*-wave velocity are very irregular and of low (<1 per cent) amplitude. In the depth interval between 1130 and 1600 km a pattern of high *P*-wave velocity that is coherent in depth is only visible below the Mariana island arc, most noticeable in Fig. 15.18(a). Although this feature is at the same geographical location as a continuous zone of high *P*-wave velocities in the transition zone and upper mantle, a connection is not evident because a coherent pattern is absent in the depth interval between 1020 and 1130 km (layer 16, Figs 15.16a).

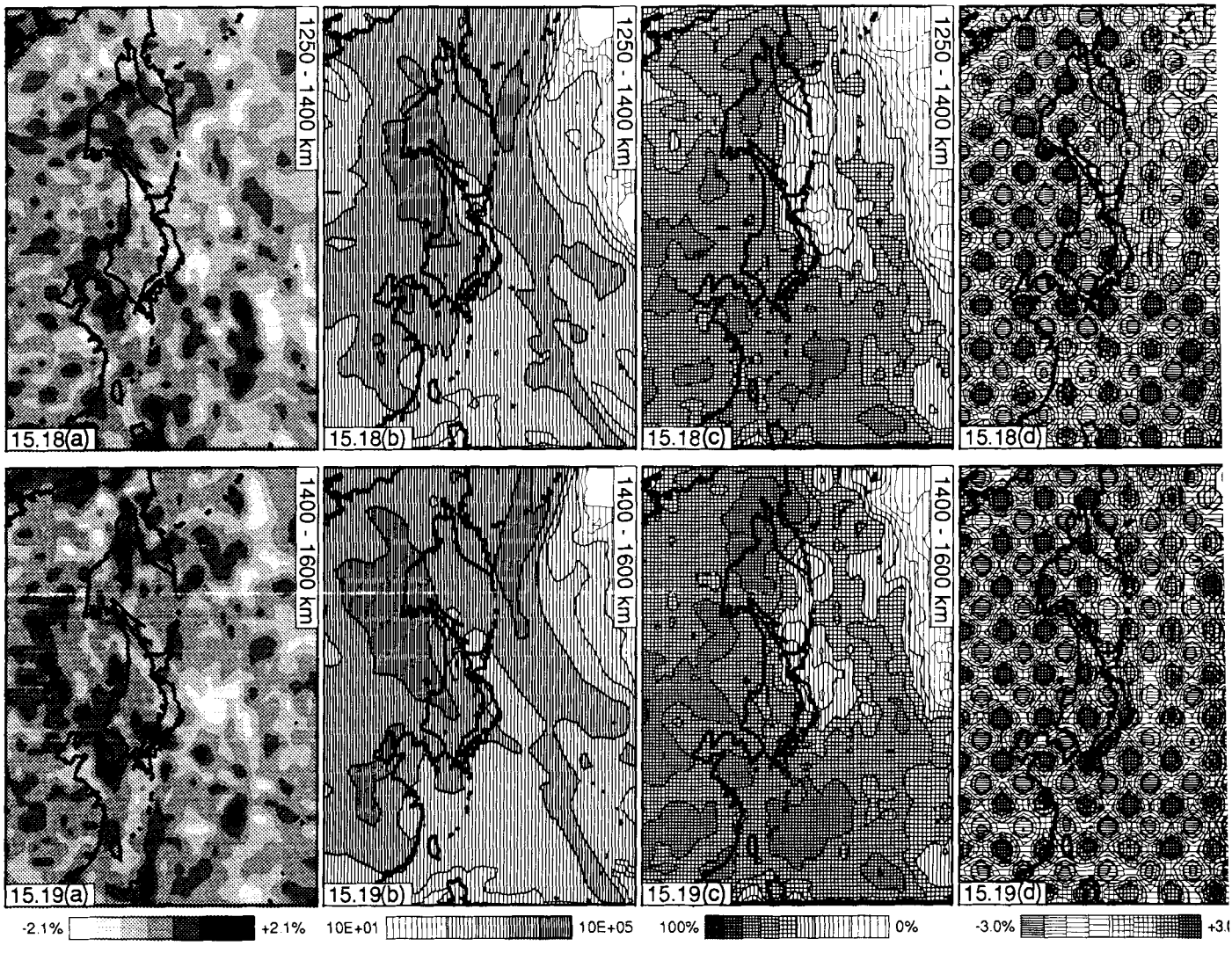

Figure 15. (*Continued.*)

4.3 Hypocentre relocation and station corrections

Hypocentre relocation. For a discussion of the second part of the solution of the inversions, the earthquake relocation parameters, we refer to Van der Hilst & Engdahl (1992). Here, we only give a summary. NWP2 and Van der Hilst & Engdahl (1992) show that for intermediate- and deep-focus earthquakes (focal depth exceeding 70 km) in the seismic zones under study, the relocation before inversion yielded relocation vectors with lengths of the order of 10 km and directions which are very systematic with regard to the position of the earthquakes in the subduction zone. The computed relocations are significant with respect to the estimated standard deviation in the relocation parameters.

For the major seismic zones in the study region, Fig. 16 displays the spatial components of the relocation vectors computed after tomographic inversion. From Fig. 16 we infer that, compared to the relocation before inversion (*cf.* Van der Hilst & Engdahl 1992), (1) the average relocation is much smaller; (2) the direction of relocation is less systematic with regard to position in the slab, and (3) the variation with focal depth of the relocation parameters is, in general, well within the standard deviation. The size of the relocation vectors computed on seismic inversion should be considered with caution, because there is no objective measure to weight the effect on traveltime residuals of source relocation versus Earth structure. By incorporating *pP* data in the inversion, however, earthquake focal depth is constrained in an educated way.

Station corrections. In this study we determined corrections for 1961 stations, located outside the geographical region under study, in order to suppress the effects of aspherical Earth structure outside the parameterized mantle volume. Station corrections published by Dziewonski & Anderson (1983) and Toy (1990) can be assumed to represent average upper mantle structure below the station as they are the result of global lower mantle studies. In contrast, the mantle region contributing to the station corrections determined in our inversions is not well defined;

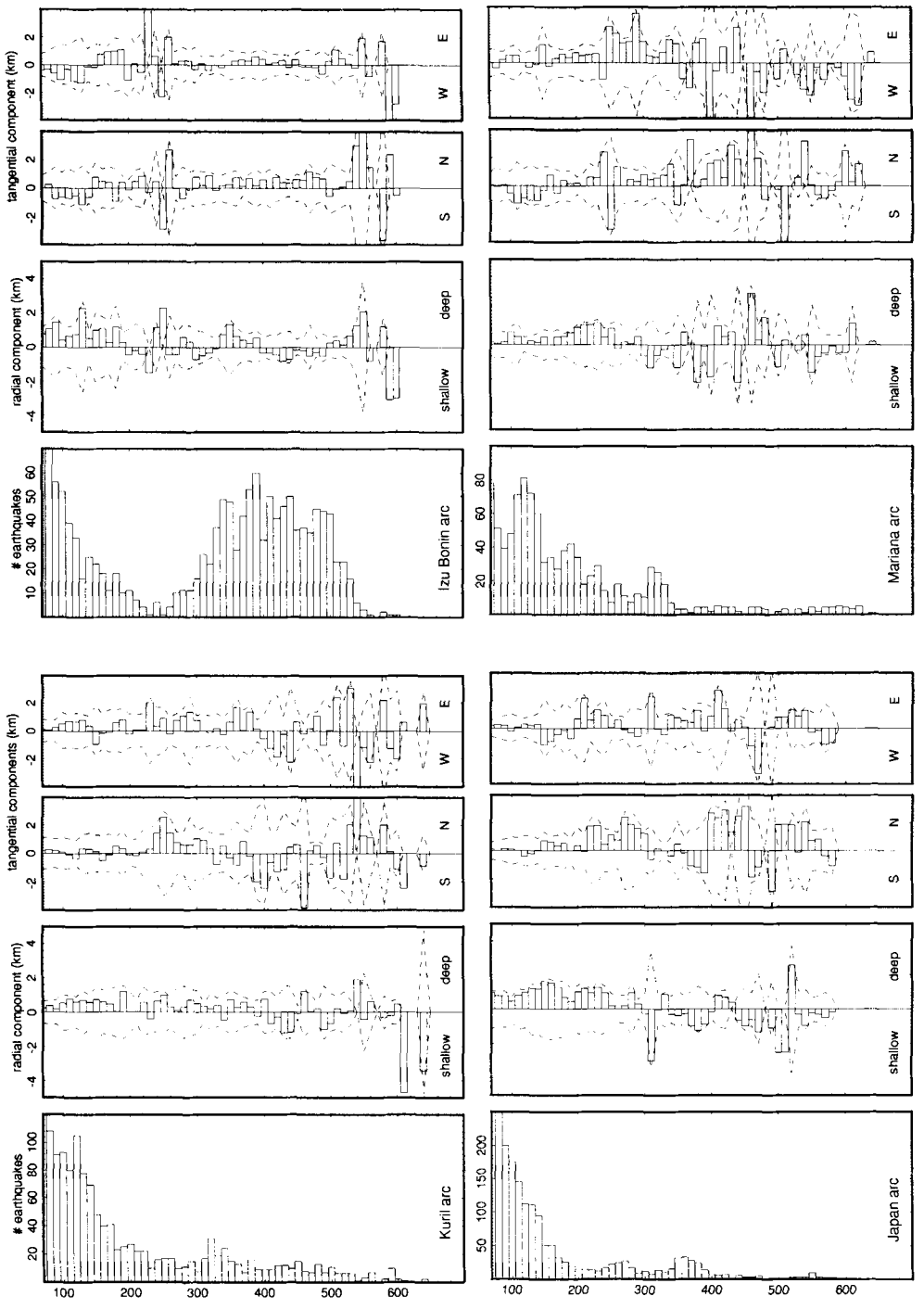

Figure 16. Spatial components of the relocation vectors for earthquakes in four major seismic zones of the northwest Pacific region. The relocation vectors are determined upon inversion of P and pP traveltime residuals for 3-D Earth structure. For each of the seismic zones the depth distribution of seismicity is given in the leftmost panel; the depth relocation (radial component) and epicentre relocation (tangential components) averaged over 10 km depth bins are presented in the other two panels. Dashed lines are drawn at $\pm\frac{1}{2}\sigma$, where σ is the standard deviation of the average relocation in a particular depth bin. We refer to Van der Hilst & Engdahl (1992) for a detailed discussion.

ray paths of the seismic waves travelling from earthquakes in the northwest Pacific region to distant stations sample Earth structure only over a limited range of azimuths and take-off angles and, hence, the corrections account for aspherical Earth structure along the entire ray path outside the parameterized mantle volume. Therefore, the corrections determined for individual stations are of only limited interest outside of this study. We present the correlations between the computed corrections, the corrections published by Toy (1990) which were used as starting value for

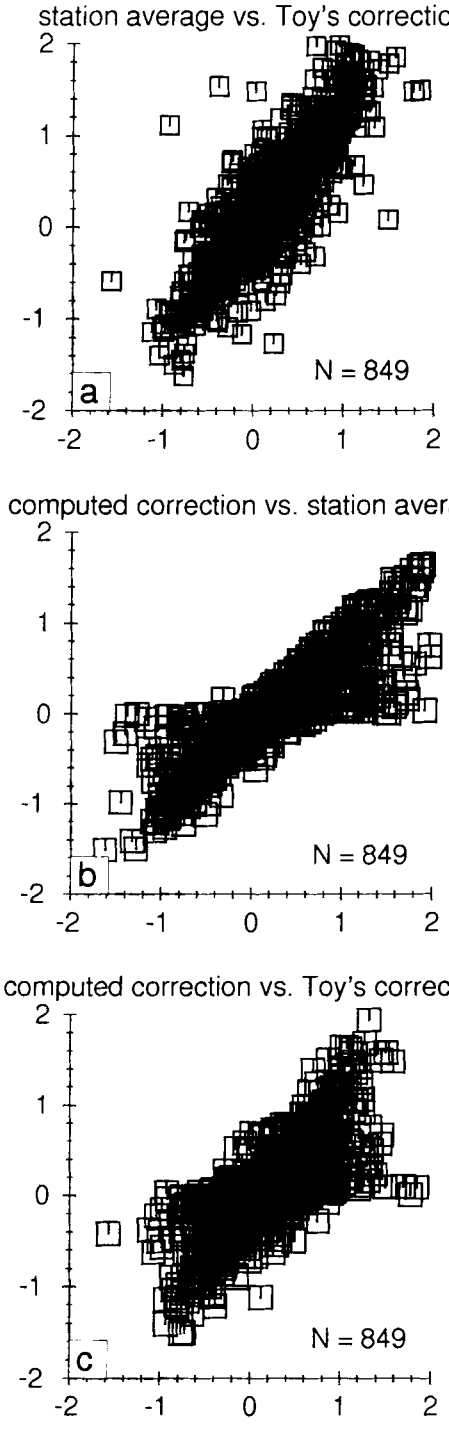

Figure 17. (a) Correlation between average station residuals and station corrections published by Toy (1990). (b) Correlation between computed station corrections after tomographic inversion and average station residuals. (c) Correlation between computed corrections and published corrections (Toy 1990).

our corrections (*cf.* Section 3.6), and the average *P*- and *pP*-wave traveltime residuals at individual stations. Fig. 17(a) shows that there is strong correlation between the average traveltime residuals and Toy's corrections. The published corrections are generally smaller than the station averages; this can be explained by our geographically limited source region (instead of a global distribution of

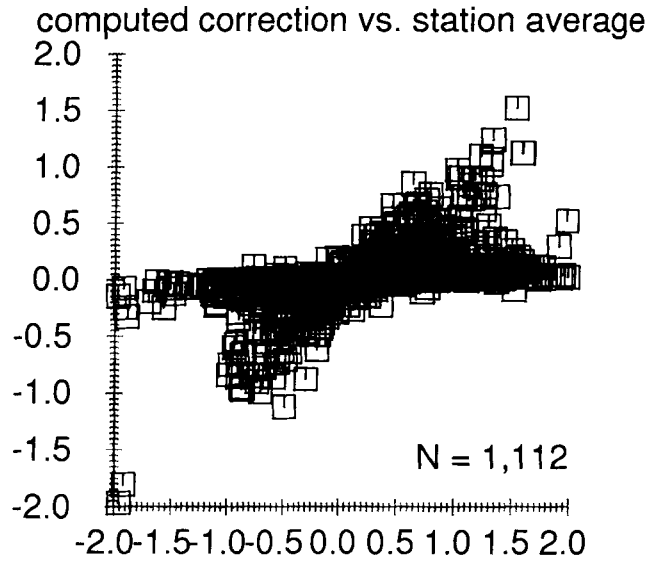

Figure 18. Same as Fig. 17(b), but for stations where no correction was published by Toy (1990).

events) and the contribution of *pP*-wave traveltime residuals to the station averages. There is a bimodality in the corrections: most corrections computed upon inversion are either of similar magnitude as the station averages or are very small (Fig. 17b). For stations for which no corrections were published small corrections predominate (Fig. 18).

5 DISCUSSION

5.1 Resolution

Resolution tests reveal high resolution of upper mantle and transition-zone structure below the central part of our study region. Structures with wavelengths of the order of the block size used for the parameterization, i.e. 100 to 150 km, are resolved below Japan, whereas structures with wavelengths of the order of 300 km are well resolved below the Kuril, Izu Bonin and Ryukyu arcs. In contrast, upper mantle structure is not resolved below continental Asia, the Pacific plate, the Aleutian arc, the central part of the Philippine Sea plate, and below part of the Mariana arc. Small-scale structure is not well resolved in depth below parts of the Izu Bonin and Mariana arcs.

Resolution of structure in the lower mantle is better than in the upper mantle and transition zone, primarily because of more homogeneous sampling by *P*- and *pP*-wave ray paths. However, also the particular design of the resolution test yields a better recovery of lower mantle structure (*cf.* Sections 4.1.3 and 4.1.4). Thus, it is unrealistic to conclude that lower mantle structures with wavelengths of the order of 100 km are well resolved. Although smoothing is applied in the inversion that 'simulates' a ray tube (Spakman & Nolet 1988), ray paths with infinitesimally small width are used. Therefore, only large-scale variations in *P*-wave velocity can be relied on for the discussion of lower mantle structure.

The spatial resolution of aspherical Earth structure obtained in our study compares favourably with that of other tomographic studies. This is mainly due to our use of a

larger number of P residuals and P-wave ray paths, and to the incorporation of pP-wave ray paths. In some regions lateral variation in the images of Earth structure coincides with variation in sampling and resolution. Where this occurs, any interpretations based on the tomographic images can only be tentative at best.

5.2 Evaluation of the iasp91 model as reference model for tomography

One-dimensional ray tracing shows that for rays bottoming in the depth range between 200 and 700 km the spatial distance between paths computed in the J–B model and paths in the iasp91 model can be as large as 200 km. This difference is large with respect to the typical cell sizes used for parameterization, and to the effects of lateral heterogeneity not accounted for in the reference model. Thus, in a linearized inversion in which the reference ray paths are not changed, iasp91 has an important advantage over the J–B model (which does not adequately represent upper mantle discontinuities) when seismic discontinuities are present in the Earth. For our regional tomographic study we could perhaps improve on the global iasp91 model, but the effect of small changes in the reference model on the ray paths is small and not likely to exceed the uncertainty due to unknown lateral heterogeneity.

Fukao *et al.* (1992) used ISC hypocentre locations and a 1-D reference model without upper mantle discontinuities that was derived from the whole mantle model of Inoue *et al.* (1990), which depicts, in turn, deviations from the Herrin model (Herrin *et al.* 1968). However, as in this study, they did not incorporate 3-D ray tracing. In general, the solution of a least-squares inversion is 'close' to the starting model used. For instance, in our solution the average anomalies at a particular depth are within a few tenths of a per cent of the iasp91 velocities (Table 1). This explains why Fukao and co-workers do not arrive at a final 1-D reference model with upper mantle discontinuities by iteratively updating the 1-D model with spherical averages of a previous 3-D model. In addition, the relocations determined upon inversion, shown in Fig. 16, are smaller and less well constrained than relocation vectors determined by an independent procedure (Van der Hilst & Engdahl 1992). Updating the reference model and source locations with results from previous inversion runs may, therefore, not be an efficient procedure to escape form a local minimum in the model space, although it will (probably) yield a better solution than with a standard model and reported hypocentres.

Of course, any spherically symmetric reference model will have two major disadvantages. First, the depth to seismic discontinuities would remain fixed. This is a severe limitation because variation in depth to the major discontinuities influences the ray paths used. The iasp91 depths of 410 and 660 km to the seismic discontinuities between upper mantle and transition zone, and transition zone and lower mantle, respectively, are in good agreement with results from stacked digital seismograms (Shearer 1990, 1991), and the analysis of *ScS* reverberations (Revenaugh & Jordan 1991). These investigations also reveal that the depth to the '660 km' discontinuity is subject to regional changes. Shearer (1991) and Shearer & Masters (1992) concluded that the '660 km' discontinuity is depressed by about 20 km below northwest Pacific island arcs. A discontinuity which is in reality deeper than specified in the reference model would result in the imaging of artificially lower P-wave velocities just below it. This may explain the low-velocity images just below the deepest seismicity of the Japan and Izu Bonin seismic zones (Fig. 15.12a). Second, with a 1-D reference model no allowance is made for ray path distortion due to lateral heterogeneity. The neglect of ray bending results in the overestimation of slab thickness (Engdahl & Gubbins 1987); 3-D ray tracing is necessary to properly assess slab width. A computer-intensive way to take into account the effects of lateral heterogeneity on traveltime and ray path is to iterate on the 3-D velocity model by updating the earthquake hypocentres and ray paths with 3-D ray tracing. Such a non-linear inversion has proven very successful in small-scale tomographic studies (Hasegawa *et al.* 1991), but to date has not been applied on a (sub)global scale. Perturbation theory could provide us, however, with a more economical way to account for the non-linear effects of lateral heterogeneity on traveltime (Snieder & Sambridge 1992).

We mentioned in Section 3.5 that there may be a bias in imaged seismic structure and hypocentre locations based on $pP-P$ times because of the continental character of the iasp91 model (Kennett & Engdahl 1991) whereas most pP reflections are located in oceanic or marginal sea regions. This problem can only be solved if the P and pP traveltimes are computed in an aspherical model that includes information about continental, stretched continental, and oceanic lithosphere. As this is not (yet) a practical possibility, we assess the problem *a posteriori* by comparing pP-wave traveltimes computed in iasp91 and in pac91. The latter is a hybrid model with a more oceanic character (Kennett 1992). In Fig. 19 we plotted the difference between the traveltimes as function of epicentral distance and focal depth. As expected, Fig. 19 shows that the pP-wave traveltime in pac91 is always faster than in iasp91.

The bias in traveltime, which can be of the order of a second, can influence our results in two ways. First, a bias to faster pP arrivals would influence $pP-P$ differential times and thus the non-linear procedure of hypocentre relocation and phase (re-)identification prior to inversion (NWP2). For the present study region we followed Kennett's conclusion that for hypocentre location below oceanic marginal sea

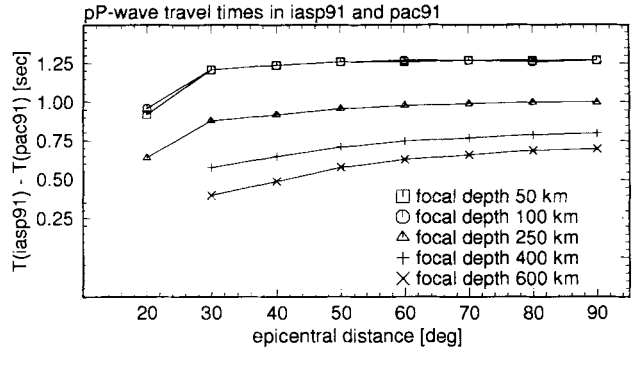

Figure 19. Difference between pP-wave traveltimes computed in the 'continental' iasp91 (Kennett & Engdahl 1991) and the more 'oceanic' pac91 (Kennett 1992).

regions 'it is probably simplest to employ the 'continental' iasp91' (Kennett 1992). Second, the difference in traveltime will result in a bias towards higher compressional velocities near the pP reflection points if these are located in oceanic or marginal sea regions. Comparison of the distribution of *pP* reflection points (Fig. 11) with the imaged seismic velocities in the uppermost layers of our model (Figs 14[1, 2]a) suggests that the bias discussed here possibly contributes to the shallow high *P*-wave velocity below Sakhalin island and southeast Japan. In general, the images are indicative of lower-than-average seismic velocity below the back-arcs of the northwest Pacific island arcs (see Section 4.2.2). This suggests that the bias due to the continental character of iasp91 is not severe, but the lateral extent of the zones of low seismic velocity below the marginal basins may be underestimated. We note that the lithosphere of the Sea of Japan and the Sea of Okhotsk is heterogeneous in that large fragments of it are of continental nature.

5.3 Aspherical mantle structure: slab morphology

An important result of our study is the difference in nature of the images of aspherical structure between the upper mantle/transition zone and the lower mantle. Apart from details, the images of structure in the upper 660 km of the Earth's interior are characterized by laterally coherent zones of high *P*-wave velocity below island arcs where subduction of the old oceanic lithosphere is known to occur. Such laterally coherent high *P*-wave velocity features are absent in the lower mantle. As discussed above, the spatial resolution of lower mantle structure is good, and coherent velocity anomalies in the lower mantle would have been recovered if present. The amplitudes of the velocity anomalies imaged in the lower mantle are smaller than in the upper mantle and transition zone. If we tentatively interpret the coherent, seismically fast regions below the northwest pacific island arcs as images of subducted lithosphere, this result argues against the undisturbed penetration of subducted slab across the transition zone into the lower mantle. To answer the question whether our results are indicative of complete decoupling between structures in the transition zone and in the lower mantle we analyse the tomographic images in more detail.

From the Kuril to the Izu Bonin arc, the zone of high *P*-wave velocities is laterally coherent to a depth of about 220 km. Below that depth, the high-velocity zone below the Kuril arc becomes increasingly discontinuous: high *P*-wave vecloities are imaged below Kamchatka and below the southern part of the Kuril arc, but the *P*-wave velocity imaged in between these regions is not significantly higher than average (iasp91). The spatial resolution is good and the sampling by *P*- and *pP*-wave ray paths fairly homogeneous. There is no significant lateral variation in seismicity at this depth (Fig. 13). With increasing depth, the zone of high seismic velocity below northern Kuril–Kamchatka remains narrow and parallel to the arc; a coherent zone with high *P*-wave velocity is reasonably well resolved to a depth of about 850 km (Fig. 5 of NWP1). Towards the south the lateral distance between the arc and the high-velocity zone increases with depth—indicating a shallower dip— and the strike of the zone changes from arc-parallel at shallow depth (Fig. 14[1–7]a) to almost east–west in the transition zone (Fig. 14[9–11]a). The image of high *P*-wave velocity below the Sea of Japan follows the seismic zone below the Sea of Japan. Below the southern part of the Kuril arc, and below the Japan and Izu Bonin arcs, the zone of high *P*-wave velocities widens dramatically in the deeper part of the transition zone, indicating a change to a subhorizontal position of the slab-like fast zone. This broadening is not observed below the northern part of the Kuril arc nor below the Mariana arc. Both the northern and, in particular, western boundary of the wide zone of high seismic velocities are well resolved, but the southeastern edge coincides with the rapid variation in both sampling by *P*- and *pP*-wave ray paths and resolution. The lateral transition of the structure from the Izu Bonin to the Mariana region can thus not be conclusively established from this study. We note that in this region the dramatic lateral variation in morphology of the high-velocity zone coincides with a seismic gap between the deep earthquakes of the Wadati–Benioff zone beneath the Izu Bonin and the Mariana arcs (Fig. 13). Below the '660 km' discontinuity no zone of high *P*-wave velocities is detected that is laterally coherent over large distances. The inversion yields, however, zones of high *P*-wave velocities that are vertically coherent across the transition zone to lower mantle depths below the Kuril–Kamchatka and the Mariana arc (see the cross-sections in NWP1). Unfortunately, the resolution of structure in these regions is less than in the mantle below the central part of the study region.

In general, our inferences about deflected slab in the transition zone are in good agreement with other recently published results of seismic imaging (Zhou & Clayton 1990; Inoue *et al.* 1990; Fukao *et al.* 1992). Deflected slab below the Izu Bonin arc was also suggested by Okino *et al.* (1989) as an explanation for unusual seismicity several hundreds of km west off the inclined seismic zone. They modelled *P*-wave traveltimes from these 'anomalous' earthquakes and concluded that the subhorizontal slab is about 3–4 per cent faster than J–B. Our results are in excellent agreement with their conclusions. Shearer (1991) and Shearer & Masters (1992) analysed $S_{660}S$–SS differential times and advocates the depression of the '660 km' discontinuity in northwest Pacific island arcs, and beneath the southern Kurils in particular (Shearer & Masters 1992); because of its endothermic nature, the phase change occurs at larger depth because of the presence of cold, deflected slab in the transition zone. In Fig. 20 we present a vertical section across the southern Kuril arc together with the topography of the discontinuity as estimated by Shearer & Masters (1992, their Fig. 7). The geographical coordinates used to construct this section are the same as used by Shearer (Shearer, personnel communication 1991). The correlation between the larger depth to the discontinuity and the presence of (deflected) slab is remarkably good. We note that this section is spatially close to that presented in Fig. 6(b) of our earlier paper (NWP1).

A deflection of the northern part of the Japan slab in the transition zone below the island of Sakhalin is in accord with seismicity (Ekstrom, Dziewonski & Ibanez 1990; Kuge 1992). Our results are not in agreement with conclusions from Kamiya *et al.* (1988); they presented images depicting Japan and Izu Bonin subduction zones which penetrate across the transition zone into the lower mantle. In an earlier

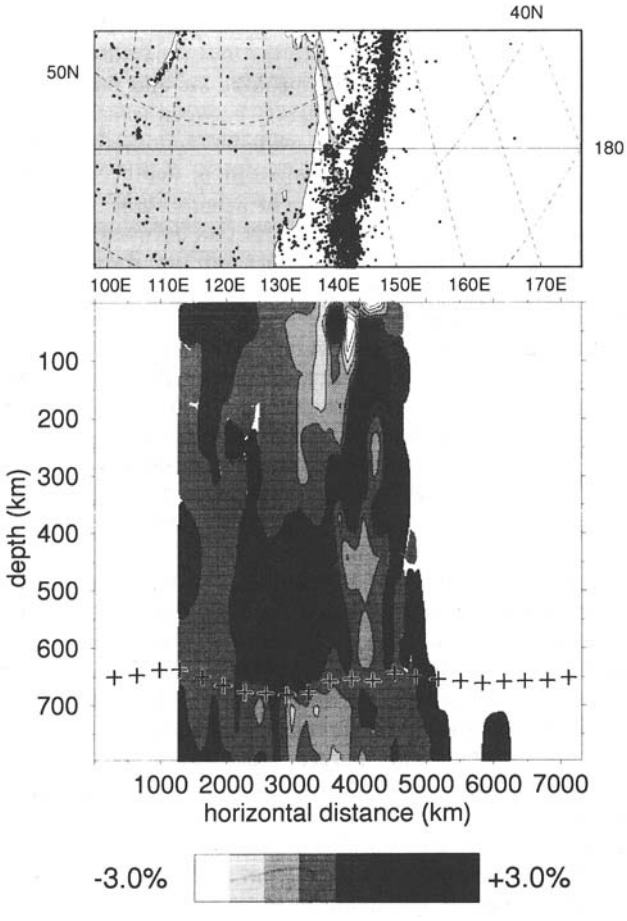

Figure 20. Vertical mantle section across the southern part of the Kuril arc, the Kuril Basin, and Sakhalin Island. Line of cross section: from (45.5 °N, 90.0 °E) to (30.0 °N, 180°). The crosses depict the topography of the '660 km' discontinuity as determined by Shearer & Masters (1992) from SS–$S_{660}S$ differential traveltimes. (Note that vertical scale is exaggerated.)

study with ISC *P* data and the J–B model as reference (Spakman *et al.* 1989) we obtained an image for the Izu Bonin slab that is very similar to the one published by Kamiya *et al.* (1988), see Fig. 4(a) in NWP1. We recall that Kamiya *et al.* used only ray paths with small take-off angles so that they would have 'missed' the aseismic horizontal parts of deflected slab. Therefore, we argue that the differences are primarily due to the use of different reference models and phase data.

It is unlikely that the image of the deflected slab represents false layering due to an incorrect global reference model. The observed velocity increase at a depth between 500 and 550 km is too high to be explained by a global discontinuity for this would contradict other seismic evidence. Besides, the increase of *P*-wave velocity at that depth is observed only locally; it is, for instance, absent below the Sea of Okhotsk where spatial resolution is also good.

Below the central part of the Sea of Japan, the images are ambiguous. High *P*-wave velocities are imaged in the lower mantle below the deflected part of the slab (Fig. 4d of NWP1) and interpretation is possible both in terms of slab deflection and slab penetration. Fast *P*-wave propagation below the deepest earthquakes of the Japan seismic zone would be consistent with conclusions by Creager & Jordan (1986), Kamiya *et al.* (1988), and Takei & Suetsugu (1989). We remark that the velocity anomaly in the lower mantle below the Japan seismic zone is laterally limited to a small region and, for the Japan arc as a whole, the images argue strongly in favour of slab deflection. Moreover, vertical resolution of structure is not very good in this region, as can be inferred from the vertical 'smearing' depicted in Figs 4(b) and (d) of the NWP1 paper. Unfortunately, with the present method and phase data available, slab morphology in that region cannot be resolved unambiguously. Furthermore, the local higher-than-average *P*-wave velocity can also be due to thermal coupling across the discontinuity (Nataf, Moreno & Cardin 1988), the presence of a cold 'megalith' (Ringwood & Irifune 1988), or a detached thermal boundary layer (Anderson 1987, 1988).

For the Kuril–Kamchatka subduction zone our results are in good agreement with residual sphere analyses of Jordan (1977), Creager & Jordan (1984, 1986), Fischer, Creager & Jordan (1988), Suetsugu (1989), and Okano & Suetsugu (1992), and with inferences based on waveform modelling (Silver & Chan 1988; Cormier 1989). For the Kuril subduction zone as a whole, the fate of the slab has been controversial. From seismic data along the depth extent of the Kuril slab is apparently difficult to establish. Differences in interpretation can partly be explained by the methods used to suppress the effects of distant Earth structure that distort the images (Gaherty, Lay & Vidale 1991; Schwartz, Lay & Grand 1991; Schwartz, Lay & Beck 1991; Okano & Suetsugu 1992). We argue here that there probably is significant lateral variation in morphology along the strike of the zone: apparent slab penetration below the northern part of the arc (Fig. 5 of NWP1), slab deflection below the Kuril Basin in the south (Fig. 20 and Fig. 6a of NWP1) and, in between, the slab is possibly strongly deformed and distorted in the transition zone (Fig. 6b of NWP1; Fischer *et al.* 1988). Our results for the Mariana subduction zone are in good agreement with Creager & Jordan (1984, 1986) but not with Okano & Suetsugu (1992) who present evidence against a lower mantle slab below the Mariana arc. Higher-than-average seismic velocities in the lower mantle below the Mariana islands are also presented by Inoue *et al.* (1990) and Fukao *et al.* (1992). We recall that the depth resolution of structure below parts of the Mariana arc is substantially less than in the other regions studied.

As a result of the incorporation of *pP*-wave ray paths the spatial resolution of structure in the upper mantle below northwest Pacific marginal basins is very good. Our inversions reveal slow *P*-wave propagation in the mantle wedge between the marginal basins and the Wadati–Benioff zones. Below the Sea of Okhotsk, *P*-wave velocities are up to 6 per cent lower than in the iasp91 model at comparable depths; below the northern part of the Philippine Sea, *P* waves propagate about 4 per cent slower than expected from iasp91. The zone of low *P*-wave velocity, which is detectable to depth of about 400 km west of the Japan and Izu Bonin zones and to about 660 km below the northern part of the Sea of Okhotsk (see Figs 5 and 6 of NWP1), is almost parallel to the zone of high velocities associated with subducted lithosphere. This result is in good agreement

with Hirahara (1977), although we yield higher amplitudes, and with results of Suyehiro & Sacks (1983) who reported evidence for low P-wave velocity below the back-arc between about 300 km in depth and the deepest earthquakes below the Sea of Japan.

5.4 Implications for models of mantle convection

From the observations described in the previous section, recently published tomographic images (Inoue *et al.* 1990; Zhou & Clayton 1990; Fukao *et al.* 1992) and other seismological studies, we propose a model in which subducted slab is deflected below the southern Kuril arc, Japan, and the northern part of the Izu Bonin arc, but locally penetrates to lower mantle depths below the Kuril–Kamchatka and the Mariana arcs. The observed variation in spatial resolution (see Section 5.1) and the fact that we do not image the actual mantle flow, but only the variation in seismic velocities, both impose limitations on interpretations of the tomographic images. For instance, without additional assumptions we cannot discriminate between slab protrusion (slab material sinks to depths beyond the average discontinuity depth without passing through the discontinuity) and slab penetration (slab material actually passes through the discontinuity and becomes part of the lower mantle). This renders tentative the interpretations from the tomographic images alone and the proposed model will, therefore, serve as a working hypothesis for discussion of the implications of our results for models of mantle convection.

Our model is consistent neither with clean, unobstructed flux across the '660 km' discontinuity nor with a complete decoupling between convective flow in upper mantle/transition zone and lower mantle, but our observations do suggest that the boundary between the transition zone and the lower mantle acts as a strong barrier for mantle flow. For the present discussion it is not so important to know whether the '660 km' is a phase change only, or whether it coincides with a gradient in density due to changes in bulk composition. Our observations do, however, exclude compositional layering with large contrasts in intrinsic density and phase transformations with large Clapeyron slopes, because that would prevent slab penetration from occurring. We prefer models of penetrative convection that allow for compositional stratification with a small (<2 per cent) increase in intrinsic density, which minimizes entrained flow, so that effectively only the negative thermally buoyant material descends into the lower mantle (Silver *et al.* 1988). Numerical modelling of homogeneous convection shows that a Clapeyron slope of $-2.0\,\mathrm{MPaC}^{-1}$ would give flow patterns consistent with our results (Christensen & Yuen 1984; Machetel & Weber 1991). With compositional layering, the Clapeyron slope required to explain intermittent mantle mixing can be somewhat shallower, which would agree well with the small variation in depth to the '660 km' discontinuity determined from P–S conversions by Wicks & Richards (1990) and Richards & Wicks (1990).

In numerical models of penetrative convection, slab penetration is still a 'hit-and-miss' proposition (Kerr 1991). Our results argue against a random process. It is a major challenge to explain why subducted lithosphere deflects in the transition zone beneath the central part of our present study region, but penetrates into the lower mantle below the northern part of the Kuril–Kamchatka arc and the Mariana arcs. If contrasts in intrinsic density between transition zone and lower mantle, combined with an endothermic phase change, influence the slab penetration depth, it is also possible that lateral variation in composition results in lateral variation in the conditions for flux between transition zone and lower mantle. Here, we do not dwell on this argument. Instead, we speculate on the relationships between plate kinematics and slab morphology across the transition zone suggested by results of the fluid dynamic experiments. The possibility to reconcile tomographic images with inferences from plate tectonic reconstructions was discussed in our NWP1 paper and the first attempt to interpret the images in this context was presented by Van der Hilst, Engdahl & Spakman (1992). A detailed model is in preparation and will be published elsewhere (Van der Hilst & Seno 1993).

Kincaid & Olson (1987) argued that slab deflection on a layer of higher viscosity would occur in the case of trench migration or 'roll back' of the slab, accompanied by back-arc spreading in the overriding plate. This model can perhaps be applied to the opening of the Kuril basin, the Sea of Japan (Kimura & Tamaki 1986; Jolivet *et al.* 1991), and the Shikoku and Parece Vela basins west of the present-day Bonin and Mariana arcs (Seno & Maruyama 1984; Ranken, Cardwell & Karig 1984; Seno 1989), but the tectonic evolution of the latter basins is still controversial (Hibbard & Karig 1990). If, in contrast, the position of the trench is more or less stable over a considerable period in geological time, the subduction can result in the accumulation of old lithosphere on a relatively small area in the transition zone. Then the positive buoyancy that subducted slab material would have in the uppermost part of the lower mantle, owing to the negative Clapeyron slope (Anderson 1987, 1988; Ringwood & Irifune 1988), can eventually be overcome and the phase transformation completed. The endothermic nature of the phase change would cause slab material to cool, become more dense than ambient lower mantle material [unless the intrinsic density contrast due to compositional layering is larger than the thermal expansion effect (Anderson 1988)], and become entrained in lower mantle convection flow. In such a model back-arc spreading can still occur, but now as the result of the retreat of the over-riding plate (Kanamori 1977; Uyeda & Kanamori 1979; Tamaki 1985). This model potentially applies to the Mariana arc, where old lithosphere of the Pacific plate has been subducted at high rates since about 43 Ma (Seno & Maruyama 1984). Until about 17 Ma the subduction process may have conformed to the retreating trench model, accompanied by the back-arc opening of the Parece Vela basin. Since that time, however, the location of the trench may have been rather stable and the present-day back-arc opening of the Mariana trough is probably due to the westward retreat of the Philippine Sea Plate (anchored slab model of Kincaid & Olson 1987).

It is interesting to note that the evolutionary models published and discussed by, for instance, Kanamori (1977), Uyeda & Kanamori (1979), and Le Pichon & Huchon (1987) implicitly bear on a transition from a (deflected) slab in the upper mantle/transition zone to a slab anchored in

the lower mantle. This transition can be understood within the framework of the tectonic evolution of the Philippine Sea region (Van der Hilst & Seno 1993).

In the context of slab penetration below the northern part of the Kuril–Kamchatka arc, as suggested by our observations, it is of relevance to note that Engebretson *et al.* (1990) estimated from plate tectonic reconstructions that more oceanic lithosphere has been subducted in the past 180 Ma below northeastern Asia than anywhere else.

We stress that these inferences are still speculative. The integration of the tectonic evolution of a particular region, e.g. the Philippine Sea, and the model of slab morphology described above is not straightforward (Hibbard & Karig 1990; Seno, personnal communication 1991) and requires further study (Van der Hilst & Seno 1993). We expect that the integration of results from seismic imaging with information from tectonic reconstructions and fluid dynamical modelling will ultimately lead to a new understanding of mantle dynamics.

6 CONCLUSIONS

Use of the iasp91 global traveltime model (Kennett & Engdahl 1991) as a reference model for *P*-wave velocities was successful for several reasons: (1) even without taking lateral heterogeneity into account, we obtained a variance for *P*-wave traveltime residuals significantly smaller than the variance of ISC *P* residuals determined from the Jeffreys–Bullen tables; and (2) we reduced confusing artefacts in the tomographic images of structure near seismic discontinuities. For our regional tomographic study we could perhaps improve on the global iasp91 model, the effect of small changes in the reference model on the ray paths is probably small and not likely to exceed the uncertainty due to unknown lateral heterogeneity.

The spatial resolution is very good in both the upper and lower mantle below the Kuril, Japan and Izu Bonin arcs. Shallow structure below the Mariana arc is less well resolved. The incorporation of *pP*-wave ray paths significantly enhanced the spatial resolution, particularly in the shallow mantle below intra-platre regions like the Philippine Sea plate, but also below island arcs. However, interpretation of the tomographic images in localized regions where the aspherical velocity variation coincides with variations in the ray sampling and spatial resolution can only be tentative.

The marked differences between the images depicting lower mantle structure and images of structure in the upper mantle and transition zone argues against clean, unobstructed continuation of subducted slab into the lower mantle below northwest Pacific island arcs. We infer that subducted slab is deflected in the transition zone below the southern Kurils, Japan and Izu Bonin arcs. This is in good agreement with the occurrence of earthquakes below the northern part of the Sea of Japan and the Philippine Sea which are well off the inclined Wadati–Benioff zones (Okino *et al.* 1989; Ekstrom *et al.* 1990; Kuge 1992), and with inferences from topography of the seismic discontinuity near 660 km (Shearer & Masters 1992). In contrast, our results do not suggest a similar slab deflection below the northern part of the Kuril–Kamchatka arc and the Mariana arc. Instead, results of our inversions are indicative of slab-like zones of high *P*-wave velocity in the lower mantle below the deepest earthquakes in the northern Kuril and Mariana subduction zones. With regard to the lateral variation in morphology of subducted slab below northwest island arcs, we concur with Fukao *et al.* (1992). Generally, however, the amplitudes of the velocity variations imaged are higher in our study.

The lateral transition from deflected slab below the northern part of the Philippine Sea plate to the steeply dipping slab which apparently penetrates into the lower mantle below the Mariana arc coincides with an absence of earthquakes with focal depth exceeding 350 km. Unfortunately, the variation in spatial resolution does not allow us to establish the transition from the Izu Bonin to the Mariana slab conclusively. The controversial interpretations of seismic data with regard to the fate of subducted slab below the Kuril arc can partly be explained by the complex morphology of the zone of high seismic velocity.

From our images we conclude that the boundary between the upper and lower mantle acts as a strong barrier for mantle flow, but that local penetration of subducted slab into the lower mantle is possible. Our results are consistent with convection models in which the '660 km' discontinuity coincides with a compositional transition characterized by a small increase in intrinsic density, a phase transformation with a shallow Clapeyron slope, or a combination. Our tomographic images thus provide support for models of penetrative convection as discussed by Silver *et al.* (1988). In order to understand why and where slab penetration or deflection at the transition zone occurs, numerical models should simulate lithospheric plates (e.g. Ricard & Vigny 1989, and references therein), include a realistic rheology (Van den Berg, Yuen & Van Keken 1991), and incorporate information about the tectonic history of important subduction zones.

ACKNOWLEDGMENTS

We thank Seth Stein for making available software to compute velocities of relative plate motion from the NUVEL_1 model, Peter Shearer for providing the information about the depth to the '600 km' discontinuity used in Fig. 20, and Brian Kennett for providing software to calculate the traveltimes used in Fig. 19. The manuscript benefited from discussions with Tetsuzo Seno and Malcolm Sambridge and from the thoughtful comments of two anonymous reviewers. R.v.d.H. thanks the theoretical geophysics group of the University of Utrecht for the hospitality and for making available their facilities. The tomographic inversions were done of the Cyber 205 computer of S.A.R.A., Amsterdam; computing time was funded by SURF, The Netherlands. During his stay in Leeds, R.v.d.H. was financially supported by NERC (QR3/7488).

REFERENCES

Adams, R. D., Hughes, A. A. & McGregor, D. M., 1982. Analysis procedure at the International Seismological Centre, *Phys. Earth planet. Inter.*, **30,** 85–93.

Aki, K., Christoffersson, A. & Husebye, E. S., 1977. Determination of the three-dimensional seismic structure of the lithosphere, *J. geophys. Res.*, **82,** 277–296.

Aki, K. & Richards, P. G., 1980. *Quantitative Seismology: Theory and Methods,* W. H. Freeman, San Francisco.

Anderson, D. L., 1987. Thermally induced phase changes, lateral heterogeneity of the mantle, continental roots, and deep slab anomalies, *J. geophys. Res.*, **92,** 13 968–13 980.

Anderson, D. L., 1988. *Theory of the Earth,* Blackwell Scientific Publications, Oxford.

Ansell, J. H. & Gubbins, D., 1986. Anomalous high-frequency wave propagation from the Tonga–Kermadec seismic zone to New Zealand, *Geophys. J. R. astr. Soc.*, **85,** 93–106.

Bolt, B. A., 1960. The revision of earthquake epicentres, focal depths, and origin times using a high-speed computer, *Geophys. J. R. astr. Soc.*, **3,** 433–440.

Buland, R., 1976. The mechanics of locating earthquakes, *Bull. seism. Soc. Am.*, **66,** 173–187.

Buland, R. & Chapman, C., 1983. The computation of seismic travel times, *Bull. seism. Soc. Am.*, **73,** 1271–1302.

Christensen, U. R. & Yuen, D. A., 1984. The interaction of subducting lithospheric slab with a chemical or phase boundary, *J. geophys. Res.*, **89,** 389–4402.

Chiu, J.-M., Isacks, B. L. & Cardwell, R. K., 1991. 3-D configuration of subducted lithosphere in the western Pacific, *Geophys. J. Int.*, **106,** 99–112.

Cormier, V., 1989. Slab diffraction of *S* waves, *J. geophys. Res.*, **94,** 3006–3024.

Creager, K. C. & Jordan, T. H., 1984. Slab penetration into the lower mantle, *J. geophys. Res.*, **89,** 3031–3049.

Creager, K. C. & Jordan, T. H., 1986. Slab penetration into the lower mantle beneath the Mariana and other island arcs of the northwest Pacific, *J. geophys. Res.*, **91,** 3573–3589.

Davies, G. F. & Richards, M. A., 1992. Mantle convection, J. *Geol.*, **100,** 151–206.

DeMets, C., Gordon, R. G., Argus, D. F. & Stein, S., 1990. Current plate motions, *Geophys. J. Int.*, **101,** 425–478.

Dziewonski, A. M. & Anderson, D. L., 1981. Preliminary Reference Earth Model, *Phys. Earth planet. Inter.*, **25,** 297–356.

Dziewonski, A. M. & Anderson, D. L., 1983. Travel times and station corrections for *P* waves at teleseismic distances, *J. geophys. Res.*, **88,** 3295–3314.

Dziewonski, A. M. & Gilbert, F., 1976. The effect of small, aspherical perturbations on travel times and a re-examination of the corrections for ellipticity, *Geophys. J. R. astr. Soc.*, **44,** 7–17.

Dziewonski, A. M., Hales, A. L. & Lapwood, E. R., 1975. Parametrically simple earth models consistent with geophysical data, *Phys. Earth planet. Inter.*, **10,** 12–48.

Ekström, G., Dziewonski, A. M. & Ibanez, J., 1990. Deep earthquakes outside slabs, (abstract) *EOS Trans. Am. geophys. Un.*, **71,** 1462.

Engdahl, E. R. & Gubbins, D., 1987. Simultaneous travel time inversion for earthquake location and subduction zone structure in the Central Aleutian Islands, *J. geophys. Res.*, **92,** 13 855–13 862.

Engdahl, E. R. Dewey, J. W. & Jugita, K., 1982. Earthquake location in island arcs, *Phys. Earth planet. Inter.*, **30,** 145–156.

Engdahl, E. R., Sleep, N. H. & Lin, M.-T., 1977. Plate effects in North Pacific subduction zones, *Tectonophysics,* **37,** 95–116.

Engdahl, E. R., Buland, R. & van der Hilst, R. D. 1993. Reprocessing of ISC phase data, *Bull. seism. Soc. Am.*, in preparation.

Engebretson, D. C., Kelly, K. P., Cashman, H. J. & Richards, M. A., 1990. Estimates for global subduction parameters since 180 Ma, (abstract) *EOS Trans. Am. geophys. Un.*, **71,** 1575.

Fischer, K. M T., Creager, K. C. & Jordan, T. H. 1988. Seismic constraints on the morphology of deep slabs, *J. geophys. Res.*, **93,** 4773–4783.

Fukao, T., Obayashi, M., Inoue, H. & Nenbai, M., 1992. Subducting slabs against stagnant in the mantle transition zone, *J. geophys. Res.*, **97,** 4809–4822.

Gaherty, J. B., Lay, T. & Vidale, J., 1991. Investigation of deep slab structure using long-period *S* waves, *J. geophys. Res.*, **96,** 16 349-16 367.

Grand, S. P., 1987. Tomographic inversion for shear velocity beneath the North American Plate, *J. geophys. Res.*, **92,** 14 065–14 090.

Grand, S. P., 1990. A possible station bias in travel time measurements reported to ISC, *Geophys. Res. Lett.*, **17,** 17–20.

Gubbins, D. & Snieder, R., 1991. Dispersion of *P* waves in subducted lithosphere: evidence for an eclogite layer, *J. geophys. Res.*, **96,** 6321–6333.

Hasegawa, A., Zhao, D., Hori, S., Yamamoto, A. & Horiuchi, S., 1991. Deep structure of the northeastern Japan arc and its relationship to seismic and volcanic activity, *Nature,* **352,** 683–689.

Herrin, E., Tucher, W., Taggart, J., Gordon, D. W. & Lobdell, J. L., 1968. Estimation of surface focus *P* travel times, *Bull. seism. Soc. Am.*, **58,** 1273–1291.

Hibbard, J. P. & Karig, D. E., 1990. Alternative plate model for the early Miocent evolution of the southwest Japan margin, *Geology,* **18,** 170–174.

Hirahara, K., 1977. A large-scale three-dimensional seismic structure under the Japan islands and the Sea of Japan, *J. Phys. Earth,* **28,** 221–241.

Hirahara, K. & Mikumo, T., 1980. Three-dimensional seismic structure of subducting lithospheric plates under the Japan islands, *Phys. Earth planet. Inter.*, **21,** 109–119.

Humphreys, E. & Clayton, R. W., 1988. Adaption of back-projection tomography to seismic travel time problems, *J. geophys. Res.*, **93,** 1073–1085.

Huppert, L. N. & Frohlich, C., 1981. The *P* velocity within the Tonga Benioff zone determined from traced rays and observations, *J. geophys. Res.*, **86,** 3771–3782.

Inoue, H., Fukao, Y., Tanabe, K., & Ogata, Y., 1990. Whole mantle *P*-wave travel-time tomography, *Phys. Earth planet. Inter.*, **59,** 294–328.

Jeffreys, H. & Bullen, K. E., 1967. *Seismological Tables,* British Association for the Advancement of Science, London.

Jolivet, L., Huchon, P., Brun, J.-P., Le Pichon, X., Chamot-Rooke, N. & Thomas, C., 1991. Arc deformation and marginal basin opening: Japan Sea as a case study, *J. geophys. Res.*, **96,** 4367–4384.

Jordan, T. H., 1977. Lithospheric slab penetration into the lower mantle beneath the Sea of Okhotsk, *J. Geophys.*, **43,** 473–496.

Kamiya, S., Miyatake, T. & Hirahara, K., 1988. How deep can be see the high velocity anomalies beneath the Japan islands? *Geophys. Res. Lett.*, **15,** 828–831.

Kanamori, H., 1977. Seismic and aseismic slip along subduction zones and their tectonic implications, in *Island arcs, deep-sea trenches, and back-arc basins,* pp. 163–174, eds Talwani, M. & Pitman, W. C., III, Maurice Ewing series 1.

Kennett, B. L. N., 1991. *IASPEI 1991: Seismological Tables,* Research School of Earth Sciences, Australian National University, Canberra, Australia.

Kennett, B. L. N., 1992. Locating oceanic earthquakes—the influence of regional models and local criteria, *Geophys. J. Int.*, **108,** 848–854.

Kennett, B. L. N. & Engdahl, E. R., 1991. Travel times for global earthquake location and phase identification, *Geophys. J. Int.*, **105,** 429–466.

Kerr, R. A., 1991. Do Plumes stir the Earth's entire mantle? *Science,* **256,** 1068–1069.

Kimura, G. & Tamaki, K., 1986. Collision, rotation, and back-arc spreading in the region of the Okhotsk and Japan seas, *Tectonics,* **5,** 389–401.

Kincaid, C. & Olson, P., 1987. An experimental study of subduction and slab migration, *J. geophys. Res.*, **92,** 13 832–13 840.

Kuge, K., 1992. Rapid-rupture and complex faulting of the May 12, 1990, Sakhalin deep earthquake: analysis of regional and teleseismic broadband data, *J. geophys. Res.*, submitted.

Machetel, P. & Weber, P., 1991. Intermittent layered convection in a model mantle with an endothermic phase change at 670 km, *Nature,* **350,** 55–57.

Moser, 1991. Shortest path calculation of seismic rays, *Geophysics,* **56,** 59–67.

Le Pichon, X. & Huchon, P., 1987. Central Japan triple junction revisited, *Tectonics,* **6,** 35–45.

Nakanishi, I., 1985. Three-dimensional structure beneath the Hokkaido–Tohuko region as derived from a tomographic inversion of *P*-arrival times, *J. Phys. Earth,* **33,** 241–256.

Nataf, H.-C., Moreno, S. & Cardin, P., 1988. What is responsible for thermal coupling in layered convection? *J. Phys. France,* **49,** 1707–1714.

Nieman, T. L., Fujita, K. & Rogers, W. J., Jr., 1986. Teleseismic mislocation of earthquakes in island arcs—theoretical results, *J. Phys. Earth,* **34,** 43–70.

Nolet, G., 1985. Solving or resolving inadequate and noisy tomographic systems, *J. comput. Phys.*, **61,** 463–468.

Nolet, G., 1987. Seismic wave propagation and seismic tomography, in *Seismic Tomography,* pp. 1–23, ed. Nolet, G., Reidel, Dordrecht.

Okano, K. & Suetsugu, D., 1992. Search for lower mantle high-velocity zones beneath the deepest Kuril and Mariana earthquakes, *Geophys. Res. Lett.*, **19,** 745–748.

Okino, K., Ando, M., Kaneshima, S. & Hirahara, K., 1989. A horizontally lying slab, *Geophys. Res. Lett.*, **16,** 1059–1063.

Olson, P., Silver, P. G. & Carlson, R. W., 1990. The large-scale structure of convection in the Earth's mantle, *Nature,* **344,** 209–215.

Paige, C. C. Saunders, M. A., 1982. LSQR: an algorithm for sparse linear equations and sparse least squares, *ACM Trans. Math. Soft.*, **8,** 43–71 and 195–209.

Ranken, B., Cardwell, R. K. & Karig, D. E., 1984. Kinematics of the Philippine Sea plate, *Tectonics,* **3,** 555–575.

Remkes, M. J. N. & Spakman, W., 1992. Seismic tomography of European upper mantle using branch ray-tracing methods, (abstract) *EOS Trans. Am. geophys. Un.,* **73,** 395.

Revenaugh, J. & Jordan, T. H., Mantle layering from ScS reverberations 2. The transition zone, *J. geophys. Res.*, **96,** 19 763–19 780.

Ricard, Y. & Bigny, C., 1989. Mantle dynamics with induced plate tectonics, *J. geophys. Res.*, **94,** 17 543–17 559.

Richards, M. A. & Wicks, C. W., Jr, 1990. *S–P* conversion from the transition zone beneath Tonga and the nature of the 670 km discontinuity, *Geophys. J. Int.*, **101,** 1–16.

Ringwood, A. E. & Irifune, T., 1988. Nature of the 650-km seismic discontinuity: implications for mantle dynamics and differentiation, *Nature,* **331,** 131–136.

Schwartz, S. Y., Lay, T & Beck, S. L., 1991. Shear wave travel-time, amplitude, and waveform analysis for earthquakes in the Kurile slab: constraints on deep slab structure and mantle heterogeneity, *J. geophys. Res.*, **96,** 14 445–14 460.

Schwartz, S. T., Lay, T. & Grand, S. P., 1991. Seismic imaging of subducted slabs: trades-off with deep path and near-receiver structure, *Geophys. Res. Lett.*, **18,** 1265–1268.

Seno, T., 1989. Philippine Sea plate kinematics, *Mod. Geol.*, **14,** 87–97.

Seno, T. & Maruyama, S., 1984. Paleogeographic reconstruction and origin of the Philippine Sea, *Tectonophysics,* **102,** 53–84.

Seno, T., Moriyama, T., Stein, S., Woods, D. F., DeMets, C., Argus, D. F. & Gordon, R. G., 1987. Redetermination of the Philippine sea plate motion, (abstract) *EOS Trans. Am. geophys. Un.*, **68,** 1474.

Shearer, P. M., 1990. Seismic imaging of upper-mantle structure with new evidence for a 520-km discontinuity, *Nature,* **344,** 121–126.

Shearer, P. M., 1991. Constraints on upper mantle discontinuities from observations of long-period reflected and converted phases, *J. geophys. Res.*, **96,** 18 146–18 182.

Shearer, P. M. & Masters, G., 1992. Global mapping of topography on the 660-km discontinuity, *Nature,* **355,** 791–795.

Silver, P. G. & Chan, W. W., 1986. Observations of body-wave multipathing from broadband seismograms: evidence for lower mantle slab penetration beneath the Sea of Okhotsk, *J. geophys. Res.*, **91,** 13 787–13 802.

Silver, P. G., Carlson, R. W. & Olson, P., 1988. Deep slabs, geochemical heterogeneity, and the large-scale structure of mantle convection: investigations of an enduring paradox, *Ann. Rev. Earth planet Sci.*, **16,** 477–541.

Snieder, R. K. & Sambridge, M., 1992. Ray perturbation theory for travel times and ray paths in 3-D heterogeneous media, *Geophys. J. Int.*, **109,** 294–322.

Spakman, W., 1988. Upper mantle delay time tomography with an application to the collision zone of the Eurasian, African and Arabian Plates, *PhD thesis,* University of Utrecht, The Netherlands.

Spakman, W., 1991. Delay-time tomography of the upper mantle below Europe, the Mediterranean, and Asia minor, *Geophys. J. Int.*, **107,** 309–332.

Spakman, W. & Nolet, G., 1988. Imaging algorithms, accuracy and resolution in delay time tomography, in Mathematical Geophysics: a survey of recent developments in seismology and geodynamics, pp. 155–188, eds Vlaar, N. J. *et al.* Reidel, Dordrecht.

Spakman, W., Stein, S., van der Hilst, R. D. & Wortel, R., 1989. Resolution experiments for NW Pacific subduction zone tomography, *Geophys. Res. Lett.*, **16,** 1097–1101.

Suetsugu, D., 1989. Lower mantle high-velocity zone beneath the Kurils as inferred from *P*-wave travel time and amplitude data, *J. Phys. Earth,* **37,** 265–295.

Suyehiro, K. & Sacks, I. S., 1983. An anomalous low velocity region above the deep earthquakes in the Japan subduction zone, *J. geophys. Res.*, **88,** 10 429–10 438.

Takei, Y. & Suetsugu, D., 1989. A high-velocity zone in the lower mantle under the Japan subduction zone inferred from precise measurements of *P*-wave arrival times, *J. Phys. Earth,* **37,** 225–231.

Tamaki, K. 1985. Two modes of back-arc spreading, *Geology,* **13,** 475–478.

Toy, K. M., 1990. Tomographic analysis of ISC travel time data for Earth structure, *PhD thesis,* University of California, San Diego, USA.

Trampert, J. & Leveque, J.-J., 1990. Simultaneous iterative reconstruction technique: physical interpretation based on the generalized least squares solution, *J. geophys. Res.*, **95,** 12 533–12 560.

Uyeda, S. & Kanamori, H., 1979. Back-arc opening and the mode of subduction, *J. geophys. Res.*, **84,** 1049–1062.

Van den Berg, A. P., Yuen, D. A. & van Keken, P. E., 1991. Effects of depth-variations in creep laws on the formation of plates in mantle dynamics, *Geophys. Res. Lett.*, **18,** 2197–2200.

Van der Hilst, R. D., 1990. Tomography with *P, PP* and *pP* delay-time data, and the three-dimensional mantle structure below the Caribbean region, *PhD thesis,* University of Utrecht, The Netherlands.

Van der Hilst, R. D. & Engdahl, E. R., 1991. On ISC *PP* and *pP* data and their use in delay-time tomography of the Caribbean region, *Geophys. J. Int.*, **106,** 169–188.

Van der Hilst, R. D. & Engdahl, E. R., 1992. Step-wise relocation of ISC earthquake hypocenters for linearized tomographic

imaging of slab structure, *Phys. Earth planet. Inter.*, **75,** 39–53.

Van der Hilst, R. D. & Seno, T., 1993. Influence of tectonic history on deep structure and penetration depth of subducted slabs, *Earth planet. Sci. Lett.*, submitted.

Van der Hilst, R. D. & Spakman, W., 1989. Importance of the reference model in linearized tomography and images of subduction below the Caribbean plate, *Geophys. Res. Lett.*, **16,** 1093–1096.

Van der Hilst, R. D., Engdahl, E. R. & Spakman, W., 1992. What can we learn about deep slab processes and mantle dynamics from tomographic images? (abstract) *EOS Trans. Am. geophys. J.*, **73,** 385.

Van der Hilst, R. D., Engdahl, E. R., Spakman, W. & Nolet, G., 1991. Tomographic imaging of subducted lithosphere below northwest Pacific island arcs, *Nature*, **353,** 37–43.

Van der Sluis, A. & van der Vorst, H. A., 1987. Numerical solution of large, sparse linear systems arising from tomographic problems, in: *Seismic Tomography*, pp. 53–87, ed. Nolet, G., Reidel, Dordrecht.

Wicks, C. W. Jr & Richards, M. A., 1990. Observed topography of the 670 km phase transition beneath the Tonga and Izu Bonin subduction zones, (abstract) *EOS Trans. Am. geophys. Un.*, **71,** 1473.

Zhao, D.-P., Horiuchi, S. & Hasegawa, A., 1990. Tomographic determination of velocity structure in and around the NE Japan, (abstract) *EOS Trans. Am. geophys. Un.*, **71,** 897.

Zhou, H.-W., 1988. How well can we resolve the deep seismic slab with seismic tomography? *Geophys. Res. Lett.*, **15,** 1425–1428.

Zhou, H.-W. & Clayton, R. W., 1990. *P* and *S* wave travel time inversion for subducting slabs under the island arcs of the northwest Pacific, *J. geophys. Res.*, **95,** 6829–6951.

Zhou, H.-W., Anderson, D. L. & Clayton, R. W., 1990. Modeling of residual spheres for subduction zone earthquakes, 1. Apparent slab penetration signatures in the NW Pacific caused by deep diffuse mantle anomalies, *J. geophys. Res.*, **95,** 6799–6827.

Zielhuis, A., Spakman, W., & Nolet, G., 1989. A reference model for tomographic imaging of the upper mantle shear velocity structure beneath Europe, in *Digital seismology and modelling of the lithosphere*, pp. 333–340, eds, R. Cassinis, Panza, G. & Nolet G., Plenum, London.